Pergamon

S0022-4073(96)00003-9

J. Quant. Spectrosc. Radiat. Transfer Vol. 55, No. 5, pp. 577–601, 1996

0022-4073/96 $15.00 + 0.00

LIGHT SCATTERING BY GAUSSIAN RANDOM PARTICLES: RAY OPTICS APPROXIMATION

K. MUINONEN,[a]† T. NOUSIAINEN,[a] P. FAST,[a] K. LUMME[a] and J. I. PELTONIEMI[b]

[a]Observatory, P.O. Box 14, FIN-00014 University of Helsinki and [b]Finnish Geodetic Institute, Geodeetinrinne 2, FIN-02430 Masala, Finland

Abstract—We model the shapes of irregular small particles using multivariate lognormal statistics (Gaussian random shape), and compute absorption and scattering cross sections, asymmetry parameters, and scattering phase matrices in the ray optics approximation. The random shape is fully described by the autocovariance function, which can be conveniently modeled by two statistical parameters: the standard deviation of radius and the correlation length of angular variations. We present an efficient spherical harmonics method for generating sample Gaussian random particles, and outline a ray tracing algorithm that can be adapted to almost arbitrary, mathematically star-like particles. We study the scattering and absorption properties of Gaussian random particles much larger than the wavelength by systematically varying their statistical parameters and complex refractive indices. The results help us understand, in part, light scattering by solar system dust particles, and thereby constrain the physical properties of, for example, asteroid regoliths and cometary comae.

1. INTRODUCTION

Light scattering by spherical and infinite circular-cylindrical particles can be studied using exact electromagnetic solutions.[1,2] Strictly, natural small particles never exhibit such simple shapes, nor any other deterministic shapes. We adopt a different, statistical approach to light scattering by small particles by describing their shapes using multivariate lognormal statistics. We emphasize that, in the spherical geometry, the Central Limit Theorem[3] holds for the lognormal probability density. In the present context, we consider the ray optics approximation and assume that the particles are much larger than the wavelength of incident light.

Peltoniemi et al[4] formulated the ray optics approximation for light scattering by stochastically rough particles using a Markovian approach: the ray path was assumed independent of the history beyond the previous interaction. They provided approximate propagation probabilities, and studied a wide selection of statistical parameters and refractive indices. As for the scattering phase matrix, their approach was constrained to computing the scattering phase function and degree of linear polarization. Here we provide a new spherical harmonics method for generating three-dimensional Gaussian random shapes, and compute full 4×4 scattering phase matrices accounting for the entire history of the ray paths.[5,6] We systematically vary the statistical parameters and refractive indices to learn general characteristics of light scattering by irregular particles much larger than the wavelength.

The ray optics approximation for irregular particles has also been studied by Mukai et al,[7] Schiffer and Thielheim,[8] Bottlinger and Umhauer,[9] and Hovenac.[10] Hovenac constrained his studies to spherical and nonspherical axisymmetric particles. Bottlinger and Umhauer presented a ray tracing algorithm and a method for three-dimensional reconstruction of particle shapes. Schiffer and Theilhein studied the effects of rough surface shadowing on the scattering characteristics of single particles. Mukai et al provided a one-dimensional radiative transfer approach to scattering by large particles with a random rough surface.

Schiffer[11–13] has further studied light scattering by statistically irregular particles. However, he described the irregular shapes using Gaussian rather than lognormal statistics. Such a shape model is realistic only for small standard deviations of radius and small correlation lengths of angular

†To whom all correspondance should be addressed.

variations. The same restricting assumption was made by, e.g., Mukai et al,[7] Bahar and Fitzwater,[14] Schertler and George,[15] and César et al.[16]

Light scattering by roughly wavelength-sized Gaussian random particles is an important future research topic. Valuable insight into light scattering by wavelength-sized and somewhat larger nonspherical particles has already been gained by applying the T-matrix method (Waterman[17]), in particular, to axially symmetric spheroidal and Chebyshev particles (e.g., Mishchenko,[18] and references therein), and via the separation of variables techniques for spheroidal particles (e.g., Asano and Sato,[19] Voshchinnikov,[20] and references therein).

Lumme and Rahola,[21] Michel,[22] and Peltoniemi[23] have worked on the discrete-dipole approximation, a distorted wave approach based on the Dyson and Bethe–Salpeter equations, and a variational volume integral technique, respectively, for light scattering by irregular particles. With additional programming effort, the T-matrix algorithms[18,24] could become applicable to non-axisymmetric particles. The various methods could be utilized for studying electromagnetic scattering by wavelength-sized Gaussian random particles.

In Sec. 2, we present the Gaussian random shape in detail, and Sec. 3 summarizes the ray optics approximation. Section 4 concentrates on the numerical methods for shape generation, ray tracing, and computation of forward diffraction. We show the main results in Sec. 5, and close the article by discussing the future prospects in Sec. 6.

2. GAUSSIAN RANDOM PARTICLE

2.1. Radius statistics

Assume that the random variables $\mathbf{s} = (s_1, \ldots, s_N)^T$ for given spherical coordinates $\Omega = (\vartheta_1, \varphi_1; \ldots; \vartheta_N, \varphi_N)^T$ obey multivariate normal statistics n_N with zero means and covariance matrix Σ_s (T is transpose):[3]

$$n_N(\mathbf{s}, \Sigma_s) = \frac{1}{(\sqrt{2\pi})^N \sqrt{\det \Sigma_s}} \exp(-\tfrac{1}{2}\mathbf{s}^T \Sigma_s^{-1} \mathbf{s}). \tag{1}$$

The covariance matrix elements are

$$\Sigma_{s,ij} = \beta^2 C_s(\gamma_{ij}), \quad i,j = 1, \ldots, N, \tag{2}$$

where β^2 is the variance, C_s is the autocorrelation function, and γ_{ij} is the angular distance between the directions i and j. We require that Σ_s be positive definite, $C_s(0) = 1$, $C_s'(0) = 0$, and that $C_s(\gamma) = C_s(\gamma + 2\pi)$.

We relate the random radius $r = r(\vartheta, \varphi)$ to $s = s(\vartheta, \varphi)$ through

$$r(\vartheta, \varphi) = \frac{a}{\sqrt{1+\sigma^2}} \exp(s(\vartheta, \varphi)). \tag{3}$$

The random variables $\mathbf{r} = (r_1, \ldots, r_N)^T$ then obey multivariate lognormal statistics l_N with equal means a, equal variance $a^2\sigma^2$, and covariance matrix Σ_r.[3,6]

$$l_N(\mathbf{r}, a, \Sigma_r) = \frac{1}{(\sqrt{2\pi})^N r_1 \cdots r_N \sqrt{\det \Sigma_s}} \exp(-\tfrac{1}{2}\mathbf{s}^T \Sigma_s^{-1} \mathbf{s}). \tag{4}$$

The elements of the matrices Σ_r and Σ_s, the corresponding autocorrelation functions C_r and C_s, and the variance σ^2 and β^2 are interrelated through

$$\begin{aligned} \Sigma_{r,ij} &= a^2[\exp(\Sigma_{s,ij}) - 1], \quad i,j = 1, \ldots, N, \\ \sigma^2 C_r &= \exp(\beta^2 C_s) - 1, \\ \sigma^2 &= \exp(\beta^2) - 1. \end{aligned} \tag{5}$$

Equations (1)–(5) completely describe the statistics of the Gaussian random shape. Thus, when the radius r is lognormally distributed, the 'logradius' s is normally distributed.

2.2. Slope

We establish a local coordinate system on the particle surface by the outward unit normal vector $\mathbf{e}_Z$, and the unit tangent vectors $\mathbf{e}_X$ and $\mathbf{e}_Y$,

$$\mathbf{e}_X = \frac{s_\vartheta \mathbf{e}_r + \mathbf{e}_\vartheta}{\sqrt{s_\vartheta^2 + 1}},$$

$$\mathbf{e}_Y = \frac{s_\varphi \mathbf{e}_r - s_\vartheta s_\varphi \mathbf{e}_\vartheta + (s_\vartheta^2 + 1)\sin\vartheta \mathbf{e}_\varphi}{\sqrt{(s_\vartheta^2 + 1)s_\varphi^2 + (s_\vartheta^2 + 1)^2 \sin^2\vartheta}},$$

$$\mathbf{e}_Z = \frac{\sin\vartheta \mathbf{e}_r - s_\vartheta \sin\vartheta \mathbf{e}_\vartheta - s_\varphi \mathbf{e}_\varphi}{\sqrt{(s_\vartheta^2 + 1)\sin^2\vartheta + s_\varphi^2}}, \tag{6}$$

where $\mathbf{e}_r$, $\mathbf{e}_\vartheta$ and $\mathbf{e}_\varphi$ are the unit vectors in the global spherical coordinate system, and s_ϑ and s_φ are the partial derivatives of the logradius. Note that the local unit vectors are completely determined by the logradius partial derivatives: introducing the logradius appears to be the natural way to model shapes in the spherical geometry.

The two perpendicular slopes

$$s_\vartheta = \frac{1}{r}\frac{\partial r}{\partial \vartheta},$$

$$\frac{1}{\sin\vartheta} s_\varphi = \frac{1}{r\sin\vartheta}\frac{\partial r}{\partial \varphi}, \tag{7}$$

are independent Gaussian random variables with zero mean and standard deviation (surface roughness)

$$\rho = \frac{\beta}{l_c}, \quad l_c = \frac{1}{\sqrt{-C_s''(0)}}, \tag{8}$$

where l_c is the correlation length. Furthermore, the slopes do not correlate with the logradius.

2.3. Shape in spherical harmonics

Three-dimensional Gaussian random shapes can be generated using a spherical harmonics expansion for the logradius, and a Legendre expansion for its autocorrelation function:[6]

$$s(\vartheta, \varphi) = \sum_{l=0}^{\infty} \sum_{m=0}^{l} P_l^m(\cos\vartheta)(a_{lm}\cos m\varphi + b_{lm}\sin m\varphi),$$

$$C_s(\gamma) = \sum_{l=0}^{\infty} c_l P_l(\cos\gamma), \tag{9}$$

where P_l^ms and P_ls are associated Legendre functions and Legendre polynomials, respectively. Making use of the addition theorem for spherical harmonics, it can be shown that, if the coefficients a_{lm} and b_{lm} are independent Gaussian random variables with zero means and equal variances

$$\beta_{lm}^2 = (2 - \delta_{m0})\frac{(l-m)!}{(l+m)!} c_l \beta^2, \tag{10}$$

the logradius will be normally distributed with zero mean and autocovariance function $\beta^2 C_s$ (δ_{mo} is the Kronecker symbol).

A convenient choice for the autocorrelation function is the spherical 'Gaussian' function

$$C_s(\gamma) = \exp\left(-\frac{2}{l_c^2 \sin^2 \tfrac{1}{2}\gamma}\right),$$

$$l_c = 2\sin(\tfrac{1}{2}\Gamma), \tag{11}$$

where Γ is the correlation angle—thus we obtain

$$c_l = (2l+1)\exp\left(-\frac{1}{l_c^2}\right) i_l\left(\frac{1}{l_c^2}\right), \quad l = 0, \ldots, \infty, \tag{12}$$

i_l being a modified spherical Bessel function. The stochastic shape is thus parameterized by σ and Γ, the relative standard deviation and the correlation angle. Note that, in our nomenclature, the correlation length and correlation angle generally differ from each other, and correlation lengths $l > 2$ do not correspond to real angles. Among other possible autocorrelation functions are the spherical 'Lorentz' and 'exponential' functions, which can be constructed analogously to the Gaussian autocorrelation function. In particular, fractal Gaussian random particles can be produced using the exponential function.

3. RAY OPTICS APPROXIMATION

The ray optics treatment derives from that by Muinonen et al,[25] Muinonen,[26] and Peltoniemi et al.[4] We describe the particle size by the mean-radius size parameter $x = ka$, where k is the wavenumber. As for the geometric optics part, a Mueller matrix is related to every ray and, at a boundary surface, reflection and refraction take place according to Snell's law and Fresnel's reflection and refraction matrices. As for the forward diffraction part, the two-dimensional silhouette is numerically computed for each sample shape, and diffraction is then ensemble-averaged in the Kirchhoff approximation.

The scattering phase matrix $\mathbf{P}$ relates the Stokes vector of the incident and scattered light; for the Gaussian random particle

$$\mathbf{I}_{\rm sca} = \frac{\sigma_{\rm sca}}{4\pi r^2}\mathbf{P}\cdot\mathbf{I}_{\rm inc},$$

$$\int_{4\pi}\frac{d\Omega}{4\pi}P_{11} = 1, \tag{13}$$

where $\sigma_{\rm sca}$ is the scattering cross section and P_{11} is the scattering phase function. For particles large compared to the wavelength, the scattering cross section and phase matrix can be divided into the forward diffraction and geometric optics parts (superscripts D and G),

$$\sigma_{\rm sca} = \sigma_{\rm sca}^{\rm D} + \sigma_{\rm sca}^{\rm G},$$

$$\mathbf{P} = \frac{1}{\sigma_{\rm sca}}(\sigma_{\rm sca}^{\rm D}\mathbf{P}^{\rm D} + \sigma_{\rm sca}^{\rm G}\mathbf{P}^{\rm G}),$$

$$\int_{4\pi}\frac{d\Omega}{4\pi}P_{11}^{\rm D} = \int_{4\pi}\frac{d\Omega}{4\pi}P_{11}^{\rm G} = 1. \tag{14}$$

In our ray optics approximation, we strictly require

$$\sigma_{\rm sca}^{\rm D} = \langle A\rangle,$$

$$\sigma_{\rm ext} = \sigma_{\rm abs} + \sigma_{\rm sca} = 2\langle A\rangle, \tag{15}$$

where $\sigma_{\rm ext}$ and $\sigma_{\rm abs}$ are the extinction and absorption cross sections, and $\langle A\rangle$ is the ensemble-averaged cross-sectional area. The absorption cross section is solely due to geometric optics: $\sigma_{\rm abs} = \sigma_{\rm abs}^{\rm G}$. The geometric optics single-particle albedo ϖ and the asymmetry parameter g are

$$\varpi = \frac{\sigma_{\rm sca}^{\rm G}}{\langle A\rangle},$$

$$g = \int_{4\pi}\frac{d\Omega}{4\pi}\cos\theta P_{11}, \tag{16}$$

where θ is the scattering angle. The asymmetry parameter can be divided into the forward diffraction and geometric optics parts $g^{\rm D}$ and $g^{\rm G}$ as in Eq. (14) for the scattering phase matrix.

In the Kirchhoff approximation,[26,27] the forward diffraction phase matrix can be written as

$$\mathbf{P}^{\mathrm{D}} \propto \frac{k^2}{4\pi\langle A\rangle}\langle|u(\theta,\phi)|^2\rangle(1+\cos\theta)^2\mathbf{1},$$

$$u(\theta,\phi)=\int_0^{2\pi}\mathrm{d}\phi'\int_0^{r(\phi')}\mathrm{d}r'r'\exp[-ikr'\sin\theta\cos(\phi-\phi')], \tag{17}$$

where the ensemble average leaves no dependence on ϕ, $\mathbf{1}$ is the 4×4 unit matrix, and $r(\phi')$ describes the silhouette of a sample Gaussian shape. The scattering phase matrix $\mathbf{P}^{\mathrm{D}}$ is finally normalized according to Eq. (14).

As for the geometric optics part, we designate the complex refractive index of the scatterer relative to the surrounding, nonabsorbing medium by m. For external incidence, we apply Snell's law in the form

$$\sin\iota = \mathrm{Re}(m)\sin\tau, \tag{18}$$

where ι and τ are the angles of incidence and refraction, respectively. When determining τ, we thus make use of $\mathrm{Re}(m)$ only, and assume that $\mathrm{Im}(m)$ has either negligible influence on τ or is large enough to entirely eliminate internal ray propagation.

For external incidence, the Mueller matrices of the reflected and refracted rays (subscripts R and T) can be obtained from

$$\mathbf{M}_{\mathrm{R}} = \mathbf{R}\cdot\mathbf{K}\cdot\mathbf{M}_{\mathrm{inc}},$$
$$\mathbf{M}_{\mathrm{T}} = \mathbf{T}\cdot\mathbf{K}\cdot\mathbf{M}_{\mathrm{inc}}, \tag{19}$$

where $\mathbf{K}$ is the rotation to the plane of incidence, and $\mathbf{R}$ and $\mathbf{T}$ are the Fresnel reflection and transmission matrices,

$$\mathbf{K}=\begin{bmatrix}1 & 0 & 0 & 0\\ 0 & \cos 2\psi & \sin 2\psi & 0\\ 0 & -\sin 2\psi & \cos 2\psi & 0\\ 0 & 0 & 0 & 1\end{bmatrix},$$

$$\mathbf{R}=\tfrac{1}{2}\begin{bmatrix}r_\parallel r_\parallel^* + r_\perp r_\perp^* & r_\parallel r_\parallel^* + r_\perp r_\perp^* & 0 & 0\\ r_\parallel r_\parallel^* + r_\perp r_\perp^* & r_\parallel r_\parallel^* + r_\perp r_\perp^* & 0 & 0\\ 0 & 0 & 2\,\mathrm{Re}(r_\parallel r_\perp^*) & 2\,\mathrm{Im}(r_\parallel r_\perp^*)\\ 0 & 0 & -2\,\mathrm{Im}(r_\parallel r_\perp^*) & 2\,\mathrm{Re}(r_\parallel r_\perp^*)\end{bmatrix},$$

$$\mathbf{T}=\tfrac{1}{2}\begin{bmatrix}t_\parallel t_\parallel^* + t_\perp t_\perp^* & t_\parallel t_\parallel^* - t_\perp t_\perp^* & 0 & 0\\ t_\parallel t_\parallel^* - t_\perp t_\perp^* & t_\parallel t_\parallel^* + t_\perp t_\perp^* & 0 & 0\\ 0 & 0 & 2\,\mathrm{Re}(t_\parallel t_\perp^*) & 2\,\mathrm{Im}(t_\parallel t_\perp^*)\\ 0 & 0 & -2\,\mathrm{Im}(t_\parallel t_\perp^*) & 2\,\mathrm{Re}(t_\parallel t_\perp^*)\end{bmatrix}, \tag{20}$$

where ψ is the rotation angle, and $r_\parallel$, $r_\perp$, $t_\parallel$, and $t_\perp$ are Fresnel's coefficients:

$$r_\parallel = \frac{m\cos\iota - \cos\tau}{m\cos\iota + \cos\tau},\quad r_\perp = \frac{\cos\iota - m\cos\tau}{\cos\iota + m\cos\tau},$$
$$t_\parallel = \frac{2\cos\iota}{m\cos\iota + \cos\tau},\quad t_\perp = \frac{2\cos\iota}{\cos\iota + m\cos\tau}. \tag{21}$$

Since the Mueller matrices in Eq. (19) interrelate flux densities that are not conserved, in practical

ray tracing, we establish the energy conservation by renormalizing the refraction coefficients in **T** so that

$$|r_\parallel|^2 + \frac{\mathrm{Re}(m^* \cos\tau)}{\cos\iota}|t_\parallel|^2 = 1,$$
$$|r_\perp|^2 + \frac{\mathrm{Re}(m \cos\tau)}{\cos\iota}|t_\perp|^2 = 1. \tag{22}$$

We treat the internal incidence analogously except that, inside the particle, rays can be totally reflected and attenuated due to absorption. Our condition for total internal reflection is $\sin\iota > 1/\mathrm{Re}(m)$, again depending on $\mathrm{Re}(m)$ only. We assume exponential absorption $\exp(-2\,\mathrm{Im}(m)k\,\Delta r)$ along the ray path (Δr is the path length), and apply the exponential attenuation factor to the entire Mueller matrix.

To summarize, rays are traced until the flux decreases below a specific cutoff value or the ray has undergone a specific number of internal or external reflections. Scattered rays carry Mueller matrices that contribute to the geometric optics scattering phase matrix. Ultimately, the cross sections and phase matrices are ensemble averages

$$\sigma_{\mathrm{sca}}^{\mathrm{G}} = \langle \sigma_{\mathrm{sca}}^{\mathrm{G}}(\{a_{lm}\}, \{b_{lm}\})\rangle,$$
$$\sigma_{\mathrm{abs}}^{\mathrm{G}} = \langle \sigma_{\mathrm{abs}}^{\mathrm{G}}(\{a_{lm}\}, \{b_{lm}\})\rangle,$$
$$\mathbf{P}^{\mathrm{G}} = \frac{1}{\sigma_{\mathrm{sca}}^{\mathrm{G}}}\langle \sigma_{\mathrm{sca}}^{\mathrm{G}}(\{a_{lm}\}, \{b_{lm}\})\mathbf{P}^{\mathrm{G}}(\{a_{lm}\}, \{b_{lm}\})\rangle, \tag{23}$$

where the random variables $\{a_{lm}\}$ and $\{b_{lm}\}$ are the spherical harmonics coefficients of the logradius in Eq. (9).

4. NUMERICAL METHODS

As for generating sample Gaussian random particles, we fixed the maximum degree $l_{\max}$ in the spherical harmonics and Legendre expansions by requiring a five-decimal-place agreement between the logradius autocorrelation function in Eq. (11) and its Legendre expansion in Eq. (9). We obtained the following simple rule for $l_{\max}$:

$$l_{\max} \approx \frac{275^\circ}{\Gamma} + 2.5. \tag{24}$$

Ray tracing was carried out within the circumscribing sphere of radius $a_>$ defined so that a negligible proportion of sample particles crossed the boundary. We typically assumed $a_> = a(1 + 4\sigma)$.

We developed a variable numerical step for ray tracing. The first goal was to bracket the interaction point, whereafter it could be efficiently determined using a bisectional search.[28] For external rays, because of star-like shapes, there is exactly one point on the surface between the origin and the ray location. Thus, if the ray were propagating toward the origin, the interaction point would be immediately bracketed by the initial location and the origin. Generalizing from this observation, we modeled the step using an ellipse that extended from the origin through the ray location to $a_>$ with the semimajor axis $a_>/2$. We read the step size from the intersection of the line of propagation and the ellipse. After trial and error, we found that the semiminor axis $0.1\Gamma/\sigma$ led to satisfactory results in most cases. For internal rays, the ellipse was taken to extend from one side of the circumscribing sphere to the other. In this case, the semimajor axis was $a_>$ and we used the same semiminor axis as for external rays. As compared to a fixed step size, the variable step speeded up the computations, though faster steps can probably still be developed.

The cross-sectional shape for diffraction computation was determined by incorporating, for the necessary set of azimuthal angles, a golden section search[28] for the maximum projected radius. The relevant region was found by systematically varying the ϑ-angle. The r'-integral in Eq. (17) was computed analytically, and the remaining φ'-integral numerically using equally spaced azimuths.

We incorporated 100,000 rays in the geometric optics computations, which secured good accuracy for the scattering and absorption cross sections and asymmetry parameters. Some statistical noise remained in the matrix elements. We allowed 9–19 internal reflections (10–20

internal chords), the smaller numbers corresponding to lower refractive indices. We found that allowing 1–2 external reflections sufficed for the present parameters. The entire 'ray trees' were traced until the relative fluxes of the 'branches' decreased below 10^{-4}. The errors due to ray termination, bracketing, and impossible normals altogether never exceeded 5% of the total energy. We used a two-degree resolution for the angular bins.

Finally, the CPU-time consumption sensitively depended on the characteristics of the particles: smaller correlation angles required longer spherical harmonics expansions and slower computation of radii, and larger radius standard deviations resulted in more frequent misses for the incident rays. The computing times for a single case varied from a few hours to two weeks on a 90 MHz Pentium Linux-workstation.

5. RESULTS

Peltoniemi et al[4] studied the effects of small and large roughness, refractive index, and absorption on the scattering phase function P_{11}^{G} and degree of linear polarization $-P_{12}^{G}/P_{11}^{G}$ in the Markovian approximation. We extend their approach to the entire scattering phase matrix accounting for the full propagation history in ray tracing. We have good overall qualitative agreement with the results by Peltoniemi et al, and will carry out a detailed comparison in another context. In the following, parts of the earlier results appear among the new results.

For Gaussian random particles, the scattering phase matrices have six degrees of freedom, and maximum eight nonzero elements. The six independent matrix elements are P_{11}^{G}, P_{12}^{G}, P_{22}^{G}, P_{33}^{G}, P_{34}^{G}, and P_{44}^{G}. The two remaining elements are $P_{21}^{G} = P_{12}^{G}$ and $P_{43}^{G} = -P_{34}^{G}$. The other matrix elements were correctly found to vanish in the numerical computations.

In Fig. 1, we show three sample Gaussian random shapes generated using Eqs. (3) and (19). The standard deviation of the radius is $\sigma = 0.10$ for all three shapes, and the correlation angle gradually decreases from $\Gamma = 90$ to 10° introducing more and more pronounced fluctuations on the particle surface. We note the simple truth that decreasing σ and increasing Γ lead toward the spherical shape.

We studied absorption for the refractive index and size parameter combinations $\mathrm{Re}(m) = 1.55$ and $\mathrm{Im}(m)$ $x = 0.0$, 0.1, 0.3, and 0.9, the radius standard deviations $\sigma = 0.05$, 0.10, and 0.20, and the correlation angle $\Gamma = 10$, 30, and 90°. In order for these results to hold, we need to have

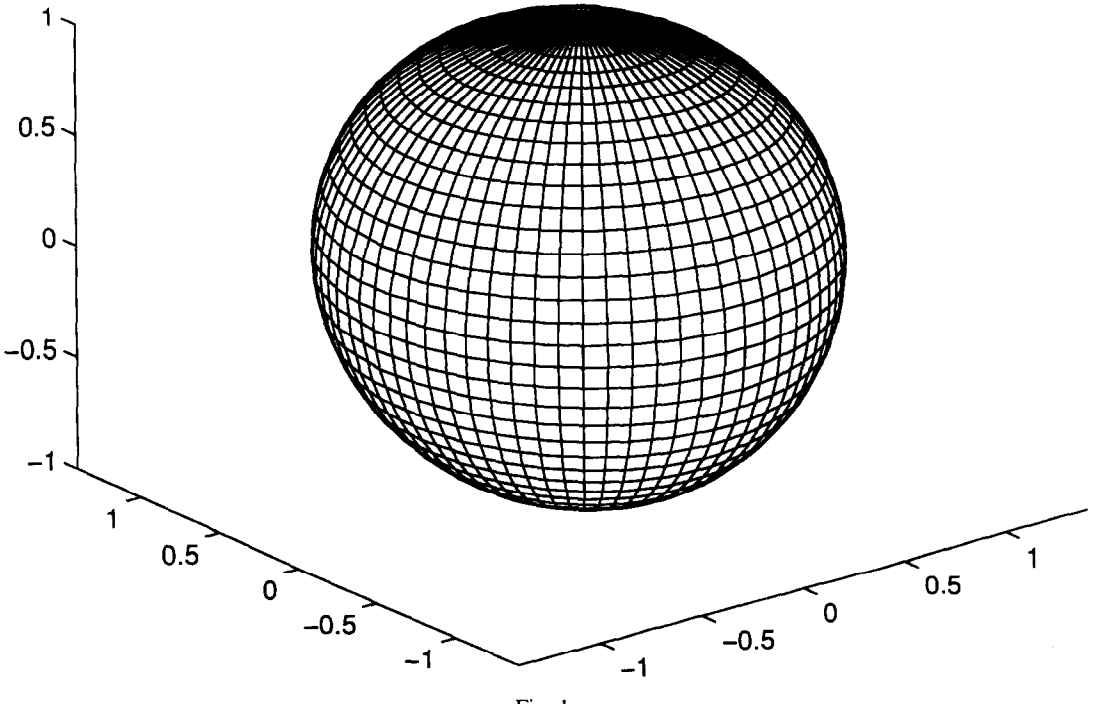

Fig. 1a

Fig. 1—*continued overleaf*

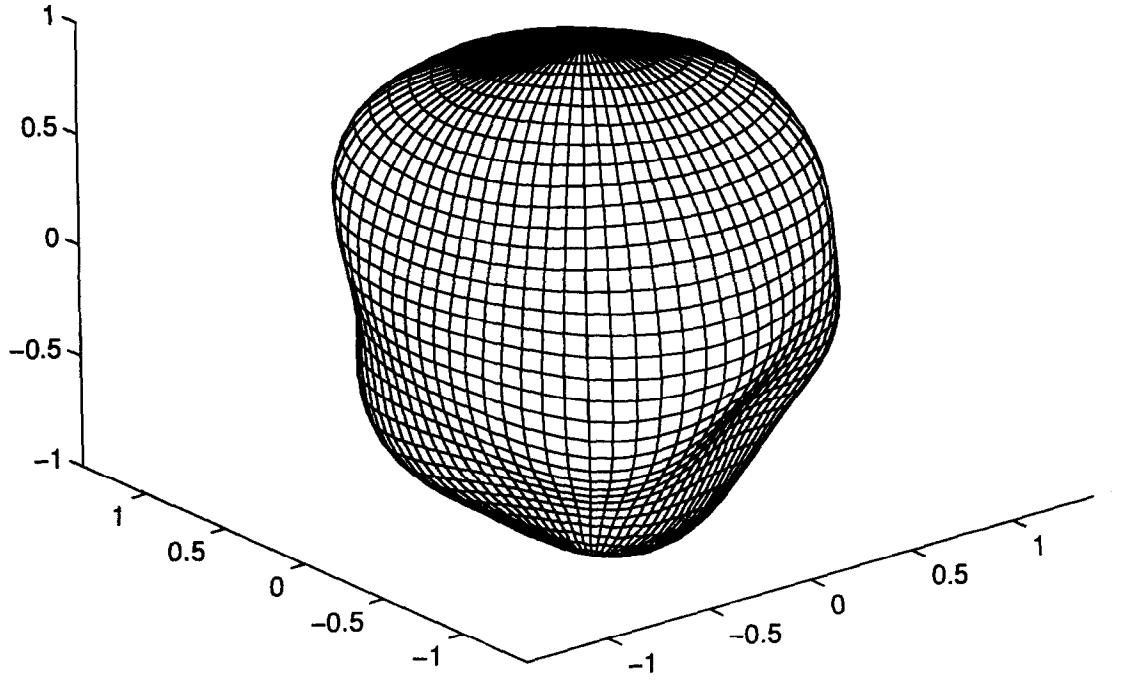

Fig. 1b

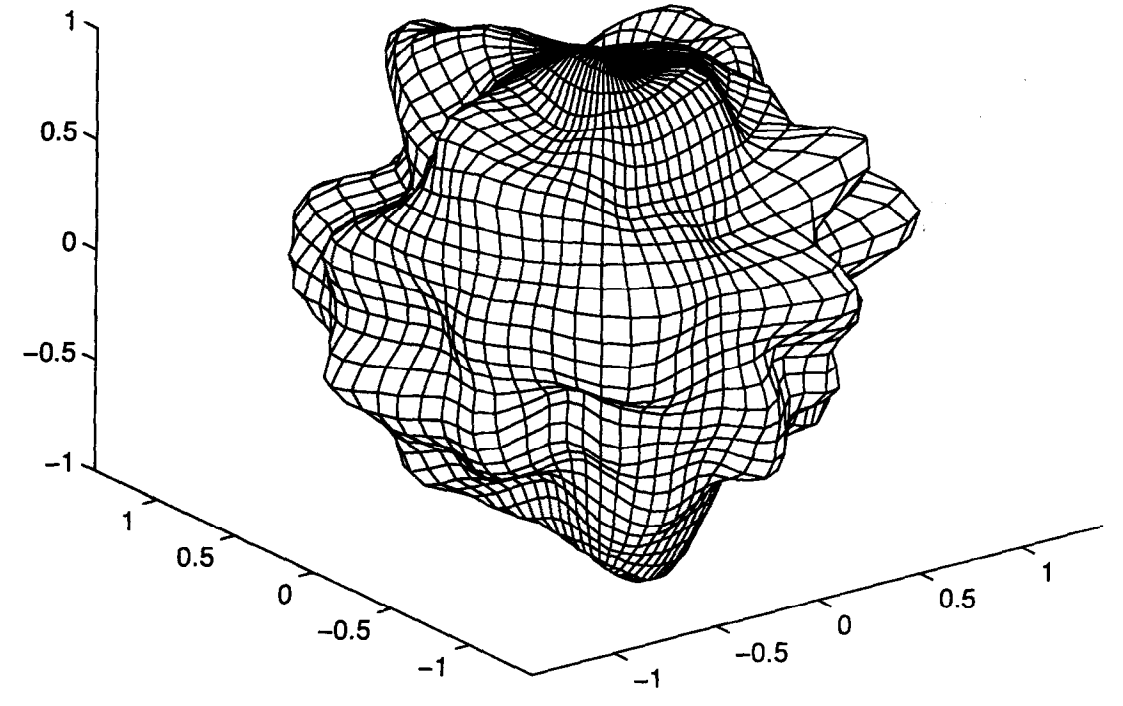

Fig. 1c

Fig. 1. Sample Gaussian random shapes with the relative standard deviation of radius $\sigma = 0.10$ and correlation angle (a) $\Gamma = 90°$, (b) $\Gamma = 30°$, and (c) $\Gamma = 10°$.

$\mathrm{Im}(m) < 0.01$, and, $x \gg 1$ and $2x|m-1| \gg 1$. Examples of $\tilde{\omega}\,\mathbf{P}^{\mathrm{G}}$ are shown in Fig. 2, and the single-particle albedos ϖ and asymmetry parameters g^{G} are presented in Tables 1 and 2, respectively. We continued by computing forward diffraction for the size parameters $x = 50$, 100, and 200, the radius standard deviations $\sigma = 0.05$, 0.10, 0.15, and 0.20, and the correlation angles $\Gamma = 10$, 20, 30, 60, 90, and 180°. The forward diffraction asymmetry parameters are given in Table 3. We then computed geometric optics results for the refractive indices $m = 1.33$, 1.55, and 2.00,

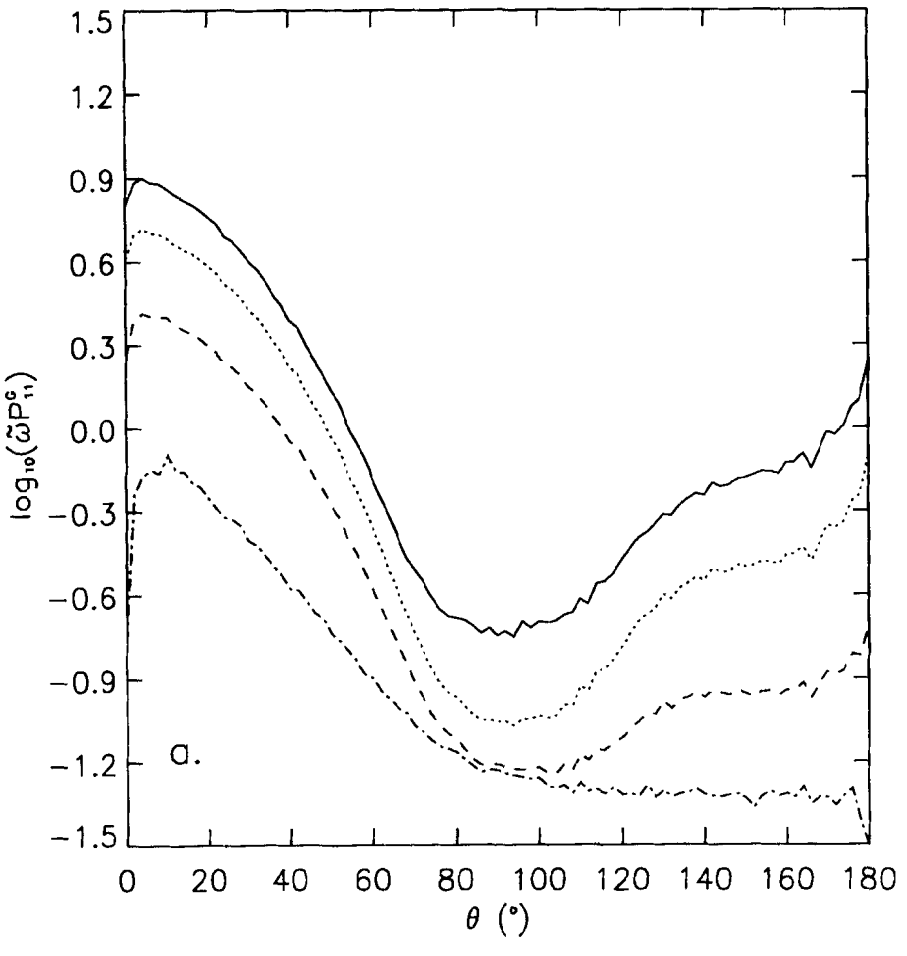

Fig. 2a

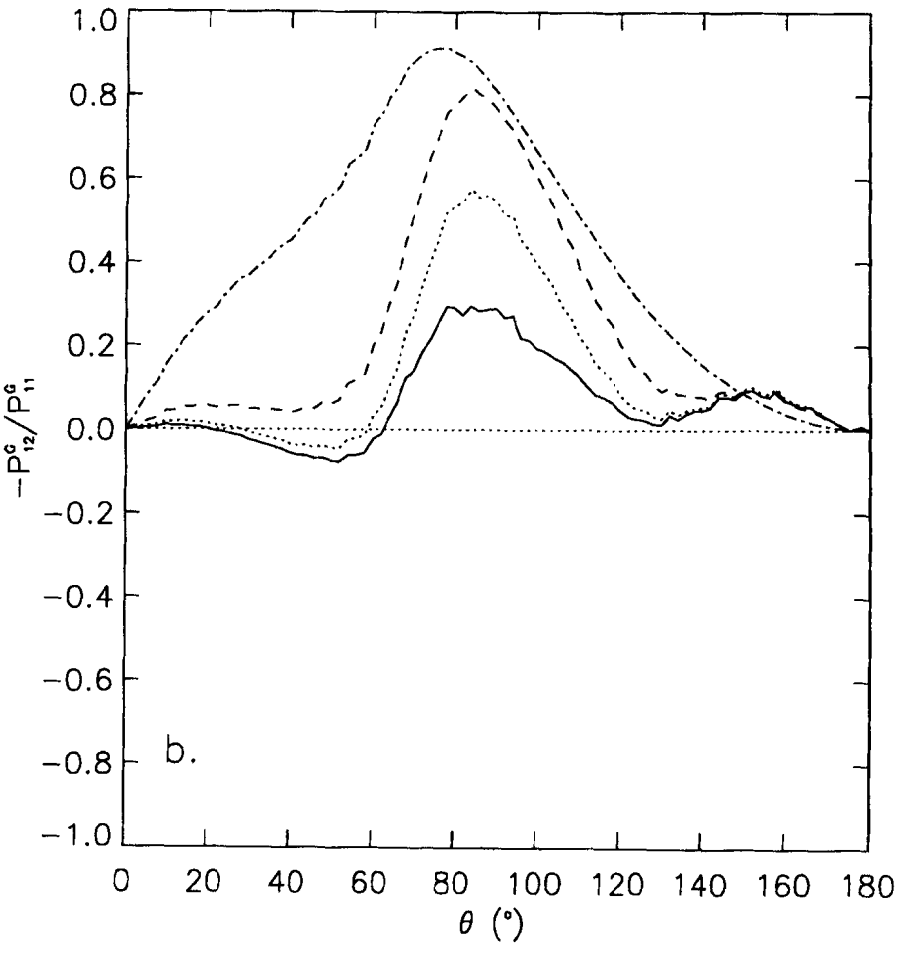

Fig. 2b

Fig. 2—*caption on p. 587*

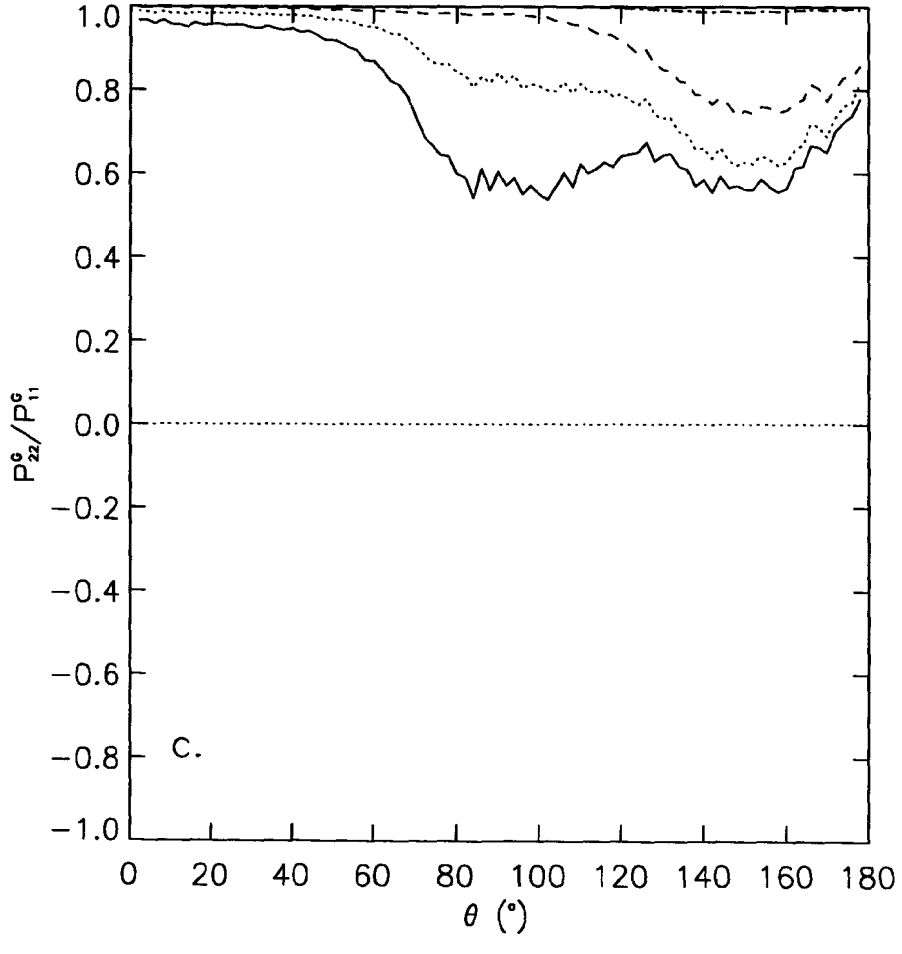

Fig. 2c

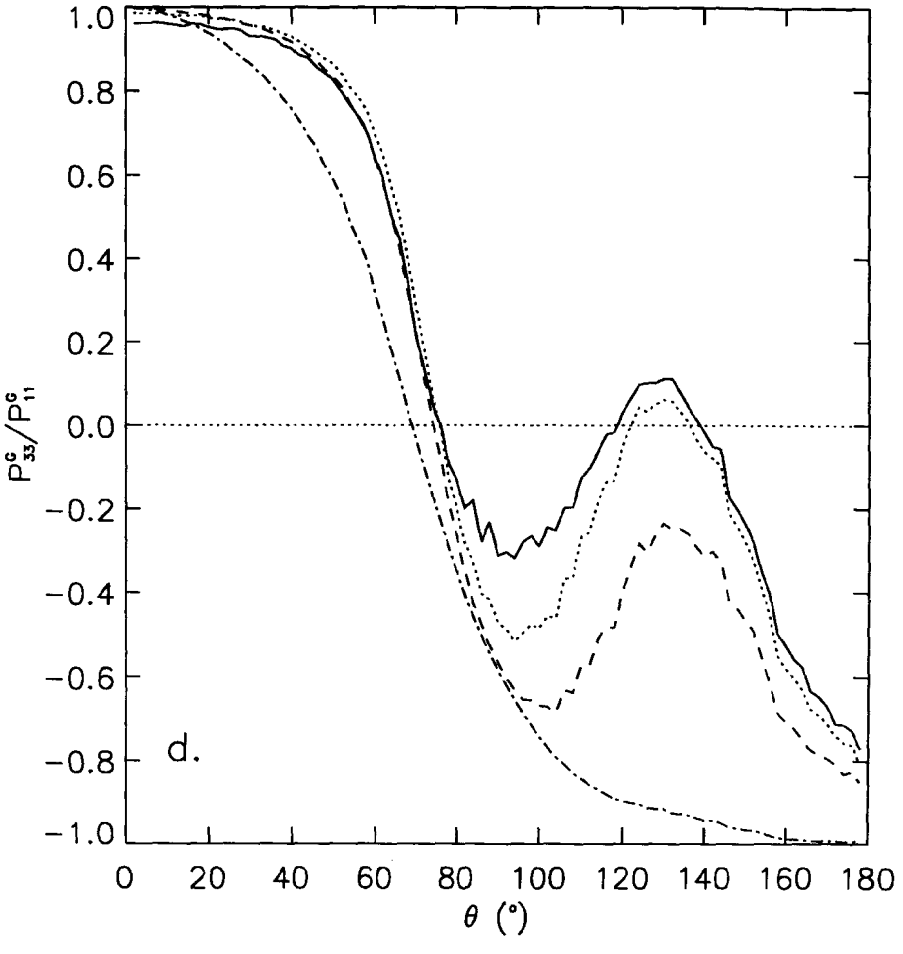

Fig. 2d

Fig. 2—*caption opposite*

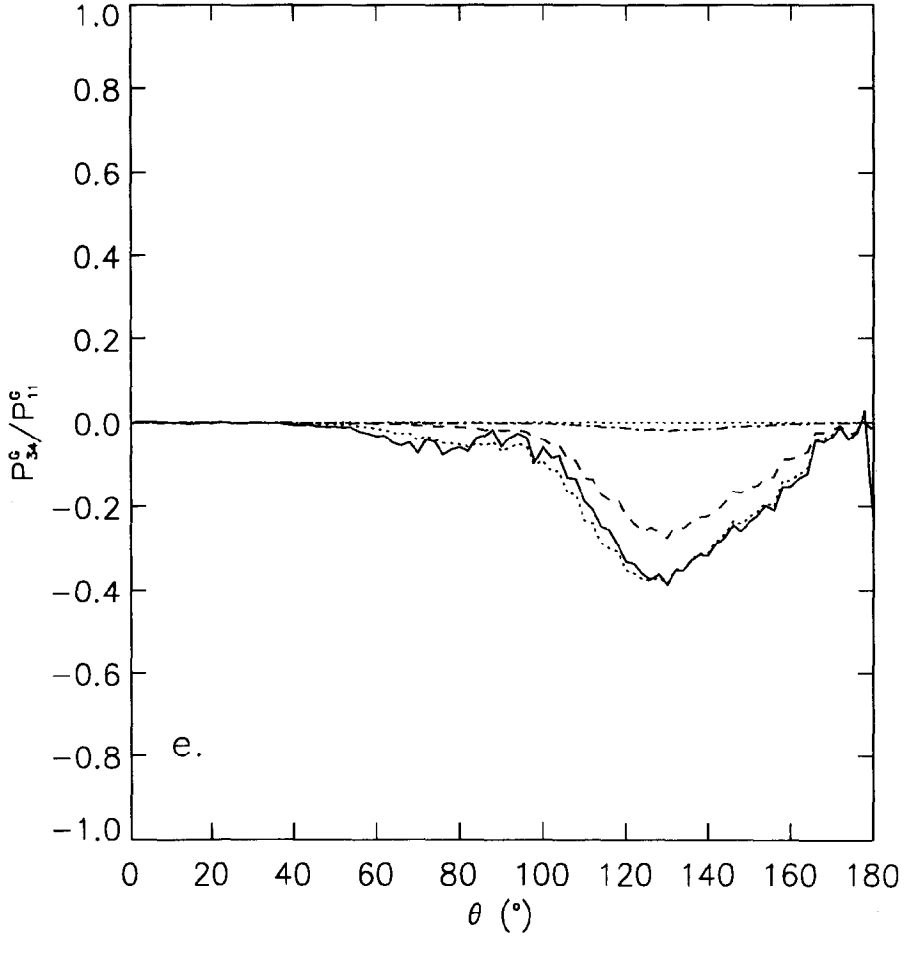

Fig. 2e

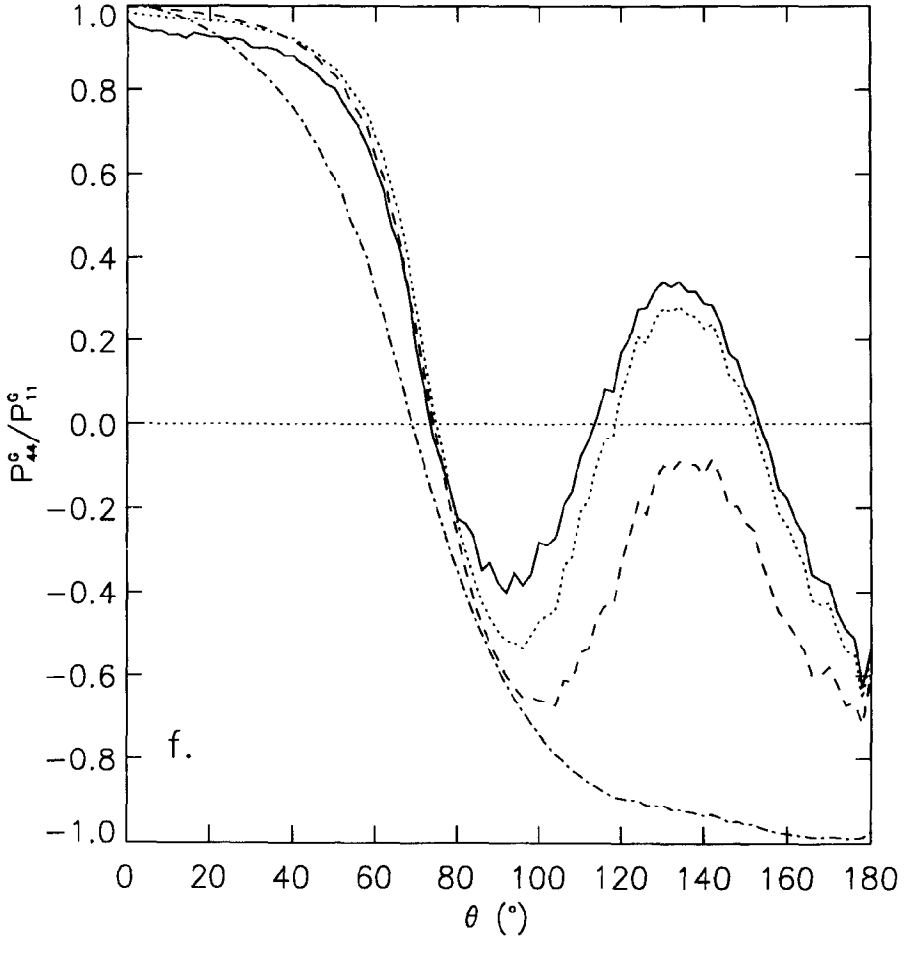

Fig 2f

Fig. 2. Geometric optics scattering phase matrices for the real part of the refractive index $\mathrm{Re}(m) = 1.55$, standard deviation $\sigma = 0.10$, and correlation angle $\Gamma = 30°$. The different lines correspond to the following products of the imaginary part of the refractive index $\mathrm{Im}(m)$ and the size parameter x: $\mathrm{Im}(m)\,x = 0.0$ (——), 0.1 (· · · ·), 0.3 (– – –), and 0.9 (· – · – · –). (a) ϖP^G_{11}, (b) $-P^G_{12}/P^G_{11}$, (c) P^G_{22}/P^G_{11}, (d) P^G_{33}/P^G_{11}, (e) P^G_{34}/P^G_{11}, and (f) P^G_{44}/P^G_{11}, where ϖ is the geometric optics single-particle albedo.

Table 1. The geometric optics single-particle albedo ϖ [Eqs. (16) and (23)] for the real part of the refractive index $\mathrm{Re}(m) = 1.55$ as a function of the standard deviation of radius σ and the correlation angle Γ.

$\mathrm{Im}(m)x$	σ, Γ								
	0.05			0.10			0.20		
	10°	30°	90°	10°	30°	90°	10°	30°	90°
0.0	1.00	1.00	1.00	1.00	1.00	1.00	1.00	1.00	1.00
0.1	0.61	0.66	0.70	0.61	0.63	0.69	0.65	0.61	0.67
0.3	0.31	0.36	0.38	0.30	0.33	0.38	0.35	0.31	0.35
0.9	0.11	0.13	0.13	0.11	0.12	0.13	0.14	0.12	0.13

Table 2. The geometric optics asymmetry parameters g^{G} [Eq. (16)] for the real part of the refractive index $\mathrm{Re}(m) = 1.55$ as a function of the standard deviation of radius σ and the correlation angle Γ.

$\mathrm{Im}(m)x$	σ, Γ								
	0.05			0.10			0.20		
	10°	30°	90°	10°	30°	90°	10°	30°	90°
0.0	0.42	0.60	0.63	0.27	0.51	0.62	0.28	0.36	0.60
0.1	0.51	0.64	0.65	0.36	0.58	0.64	0.36	0.46	0.63
0.3	0.57	0.65	0.64	0.45	0.61	0.64	0.45	0.54	0.63
0.9	0.42	0.48	0.48	0.36	0.47	0.48	0.45	0.46	0.47

Table 3. The forward diffraction asymmetry parameter g^{D} as a function of the size parameter $x = 2\pi a/\lambda$, standard deviation of radius σ, and the correlation angle Γ.

x	σ	Γ					
		10°	20°	30°	60°	90°	180°
50	0.05	0.990	0.990	0.990	0.990	0.990	0.990
	0.10	0.989	0.990	0.990	0.990	0.990	0.990
	0.15	0.989	0.990	0.990	0.990	0.990	0.990
	0.20	0.989	0.990	0.990	0.986	0.988	0.990
100	0.05	0.995	0.995	0.995	0.995	0.995	0.995
	0.10	0.994	0.995	0.995	0.995	0.995	0.995
	0.15	0.995	0.995	0.995	0.994	0.995	0.995
	0.20	0.994	0.995	0.995	0.991	0.993	0.995
200	0.05	0.998	0.997	0.998	0.998	0.998	0.998
	0.10	0.997	0.997	0.998	0.998	0.998	0.998
	0.15	0.997	0.997	0.998	0.997	0.998	0.998
	0.20	0.997	0.998	0.998	0.994	0.995	0.998

Table 4. The geometric optics asymmetry parameter g^{G} as a function of the refractive index m, standard deviation of radius σ, and correlation angle Γ.

m	σ	Γ					
		10°	20°	30°	60°	90°	180°
1.33	0.05	0.55	0.69	0.73	0.76	0.77	0.77
	0.10	0.47	0.56	0.64	0.74	0.76	0.77
	0.15	0.49	0.51	0.59	0.72	0.75	0.76
	0.20	0.51	0.50	0.56	0.70	0.74	0.76
1.55	0.05	0.42	0.57	0.60	0.63	0.63	0.63
	0.10	0.27	0.41	0.51	0.60	0.62	0.62
	0.15	0.26	0.31	0.42	0.57	0.61	0.62
	0.20	0.28	0.29	0.36	0.54	0.60	0.62
2.00	0.05	0.26	0.39	0.41	0.42	0.43	0.43
	0.10	0.11	0.25	0.34	0.39	0.41	0.42
	0.15	0.10	0.15	0.24	0.37	0.40	0.42
	0.20	0.09	0.12	0.18	0.34	0.38	0.41

and the same radius standard deviations and correlation angles as for diffraction above. Examples of the geometric optics scattering phase matrices $\mathbf{P}^{\mathrm{G}}$ are given in Figs. 2–5, and the asymmetry parameters are collected in Table 4. We thus have results for altogether 99 different combinations of the parameters (Tables 1, 2, and 4, accounting for the overlap for non-absorbing particles).

The asymmetry parameters g^{D} for forward diffraction systematically increase for increasing mean-radius size parameter x (Table 3). g^{D} is quite independent of the statistical parameters. However, toward larger standard deviations σ and for the correlation angle $\Gamma = 60°$, the asymmetry parameters differ from the neighboring values. Why this happens requires further studies: it could be an artifact due to insufficient statistical averaging.

In what follows, we analyse the cross sections, asymmetry parameters, and geometric optics scattering phase matrix elements in detail as functions of the refractive index m, radius standard deviation σ, and correlation angle Γ. However, we first summarize some general results. When varying the standard deviation of radius σ, we observed the following (cf. Fig. 3):

- For absorbing particles, increasing σ decreases ϖ (Table 1).
- For both absorbing and non-absorbing particles, g^{G} practically always decreases for increasing σ (Tables 2 and 4).
- Increasing σ efficiently destroys the rainbow features.
- For small Γ and increasing σ, the matrix elements become insensitive to changes in σ. It remains to be seen whether the elements, in fact, converge toward some limiting patterns for large σ.
- There are nodes in some of the matrix elements, i.e., angles where the elements are practically independent of σ.
- Toward larger Γ, changing σ less affects the matrix element ratios $P_{ij}^{\mathrm{G}}/P_{11}^{\mathrm{G}}$.
- Increasing σ shifts features forward in scattering angle, in particular, for small Γ. The only exception is $P_{33}^{\mathrm{G}}/P_{11}^{\mathrm{G}}$ for $m = 2.00$, for which backward scattering features tend to move backward.
- Increasing σ flattens the matrix elements, in particular, for small Γ: the minima and maxima become shallower. Furthermore, the ratios $-P_{12}^{\mathrm{G}}/P_{11}^{\mathrm{G}}$ and $P_{44}^{\mathrm{G}}/P_{11}^{\mathrm{G}}$ become shallower for increasing σ.
- In the matrix element ratios, the forward scattering regime is insensitive to changes in σ. The exception is $P_{14}^{\mathrm{G}}/P_{11}^{\mathrm{G}}$ for $m = 2.00$, in which case increasing σ decreases the curves.

When varying the correlation angle Γ, we observed the following (cf. Fig. 4):

- For absorbing particles, increasing Γ typically increases ϖ (Table 1).
- For both absorbing and non-absorbing particles, g^{G} usually increases for increasing Γ (Tables 2 and 4).
- Increasing Γ shifts features backward in scattering angle, as the random shape approaches a sphere.
- Increasing Γ tends to enhance features in the matrix element ratios. The exceptions are $P_{22}^{\mathrm{G}}/P_{11}^{\mathrm{G}}$ and $P_{34}^{\mathrm{G}}/P_{11}^{\mathrm{G}}$, which tend toward unity and zero, respectively, that are the values for a non-absorbing sphere in the geometric optics approximation.

When varying the refractive index m, we observed the following (cf. Figs. 2 and 5):

- Naturally, ϖ decreases for increasing absorption (Table 1).
- For increasing $\mathrm{Im}(m)x$, g^{G} first increases and then decreases (Table 2).
- For increasing $\mathrm{Re}(m)$, g^{G} always decreases (Table 4).
- For increasing absorption, the matrix elements become simpler and converge toward those from external reflection only.
- Increasing $\mathrm{Re}(m)$ tends to shift features backward in scattering angle.
- Increasing $\mathrm{Re}(m)$ decreases forward scattering and increases backward scattering, generally neutralizing the scattering phase function.

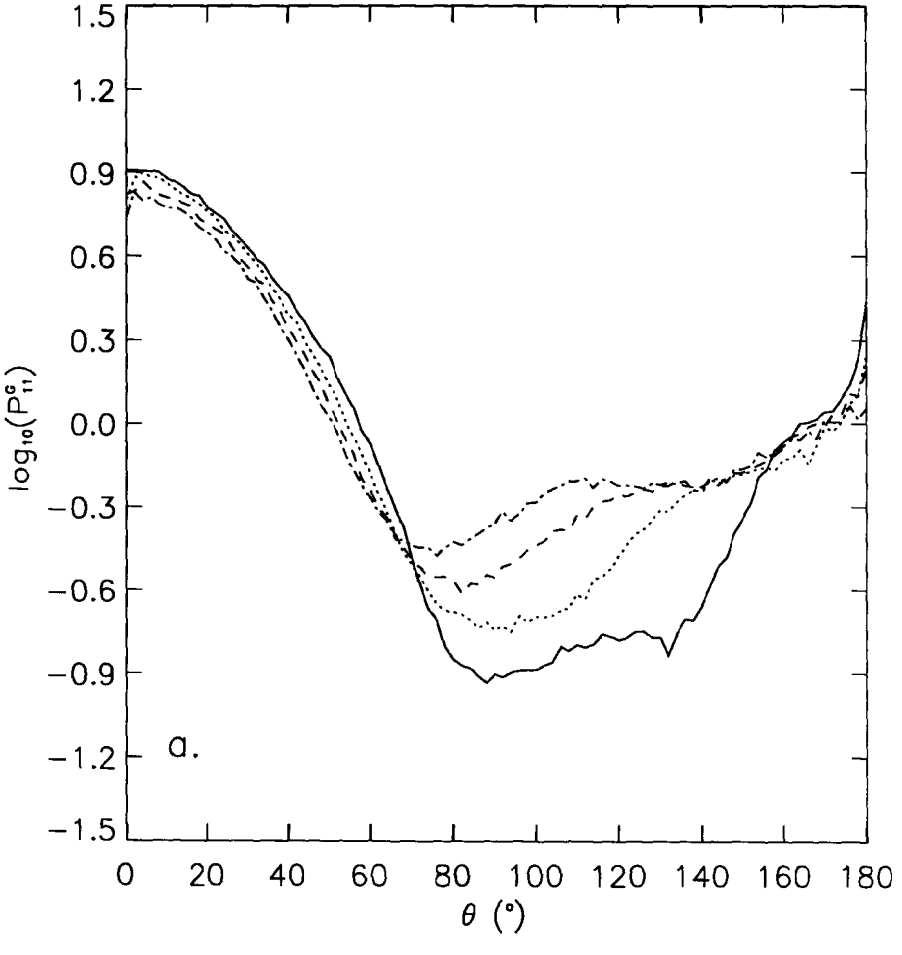

Fig. 3a

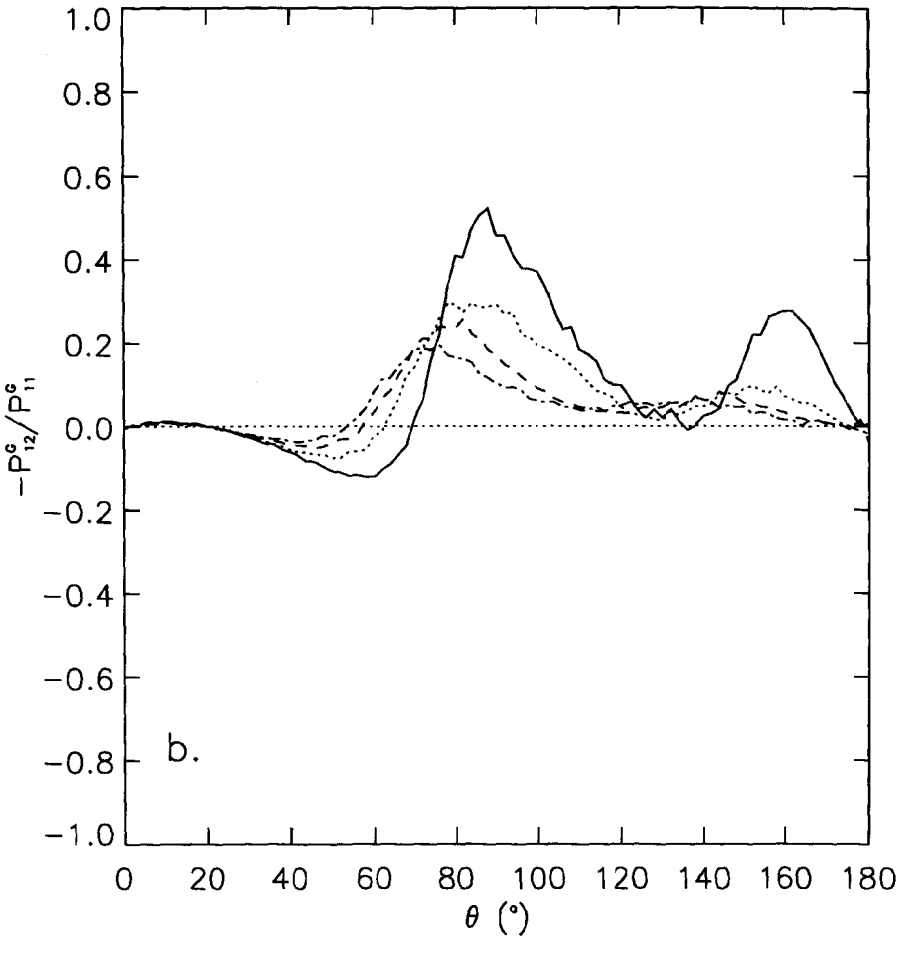

Fig. 3b

Fig. 3—*caption on p. 592*

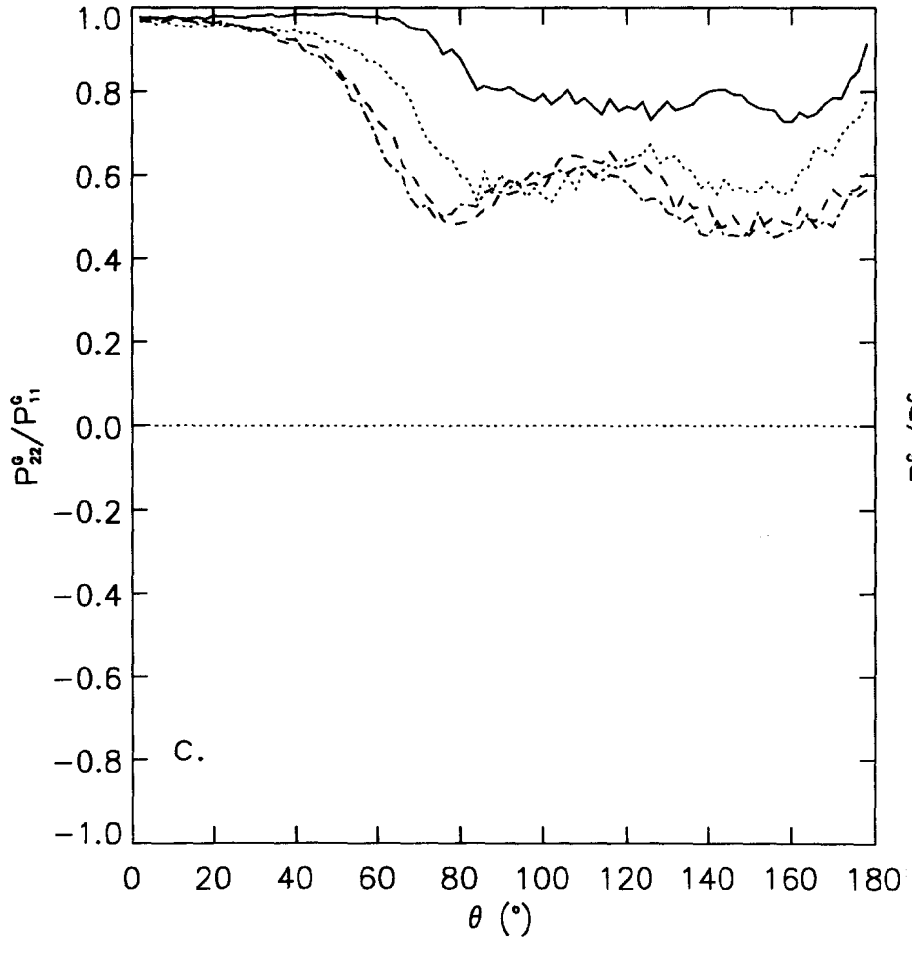

Fig. 3c

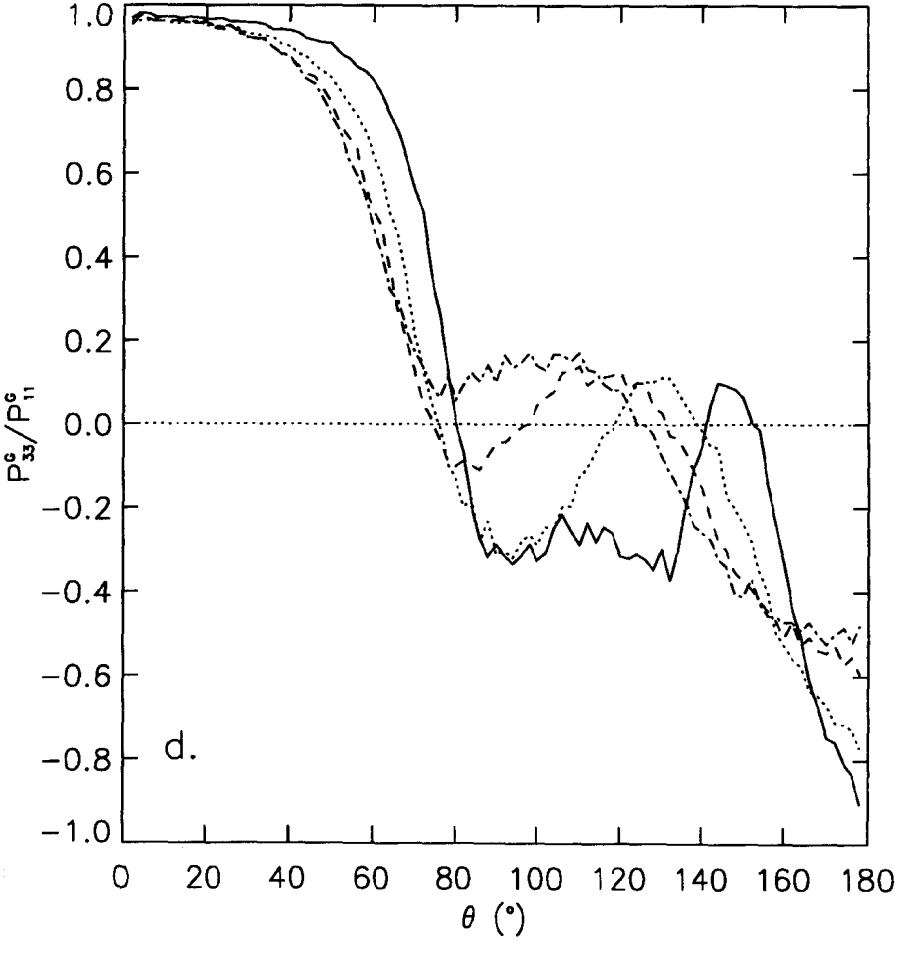

Fig. 3d

Fig. 3—*caption overleaf.*

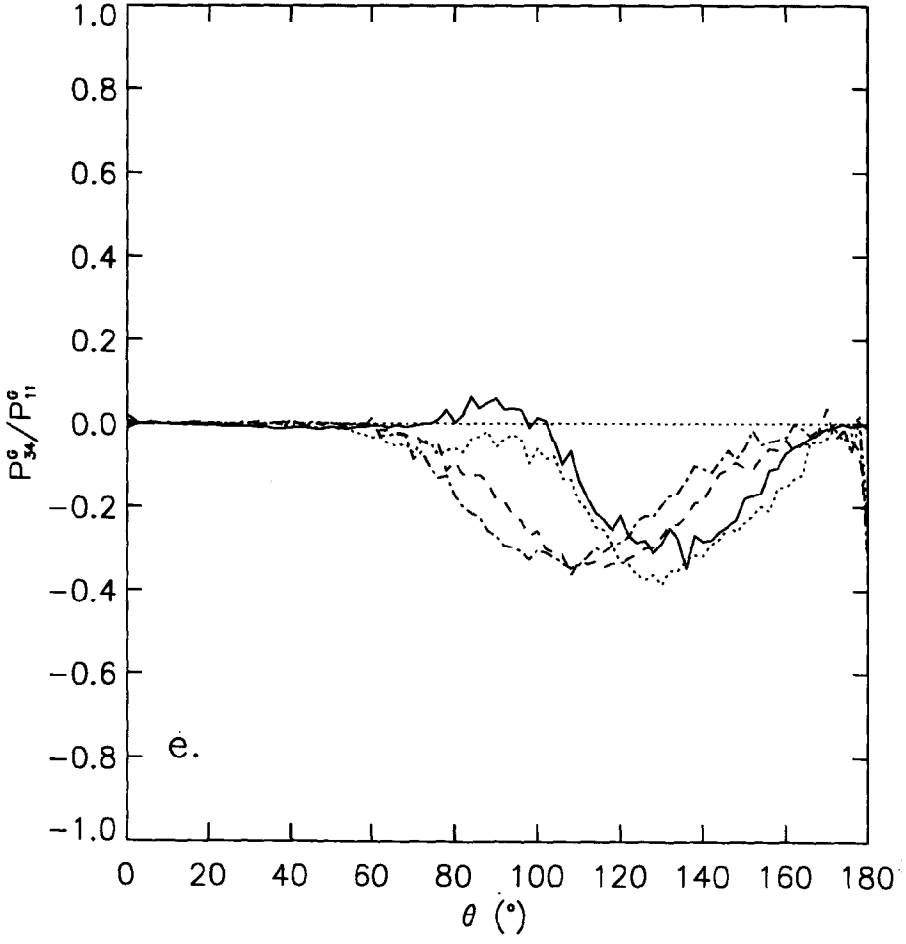

Fig. 3e

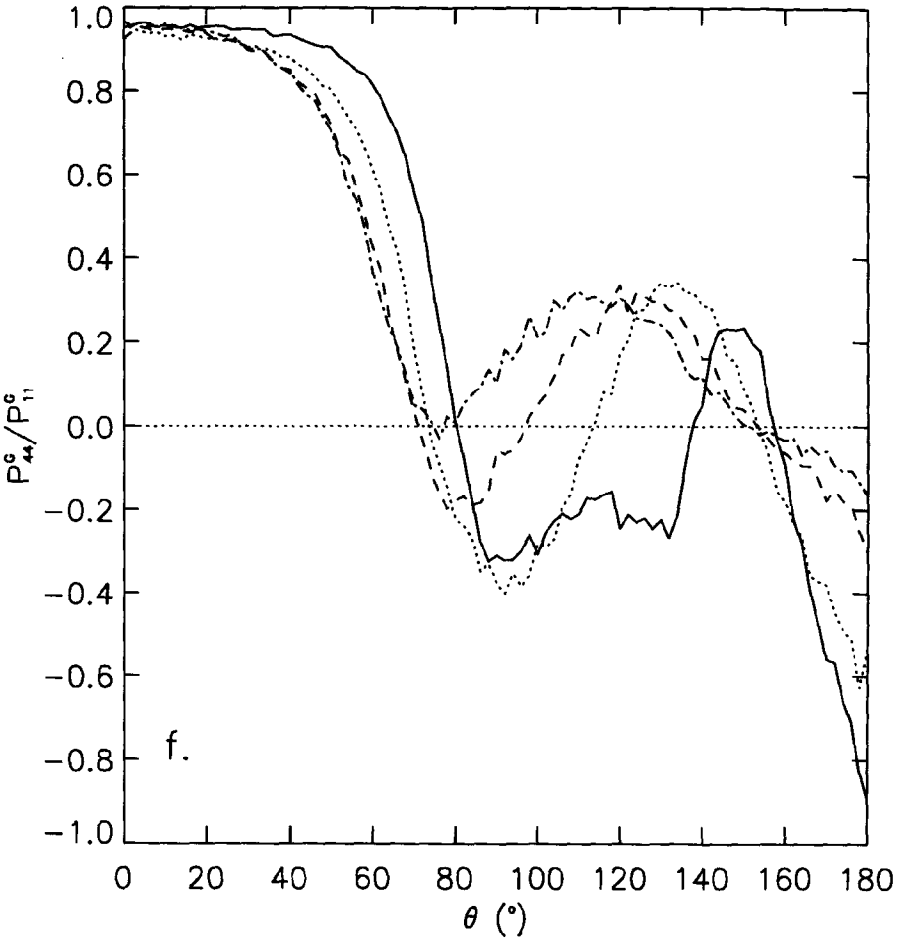

Fig. 3f

Fig. 3. Geometric optics scattering phase matrices for the refractive index $m = 1.55$ and correlation angle $\Gamma = 30°$. The different lines correspond to the standard deviations $\sigma = 0.05$ (——), 0.10 (· · · ·), 0.15 (– – – –), and 0.20 (– · – · – · –). (a) P_{11}^G, (b) $-P_{12}^G/P_{11}^G$, (c) P_{22}^G/P_{11}^G, (d) P_{33}^G/P_{11}^G, (e) P_{34}^G/P_{11}^G, and (f) P_{44}^G/P_{11}^G.

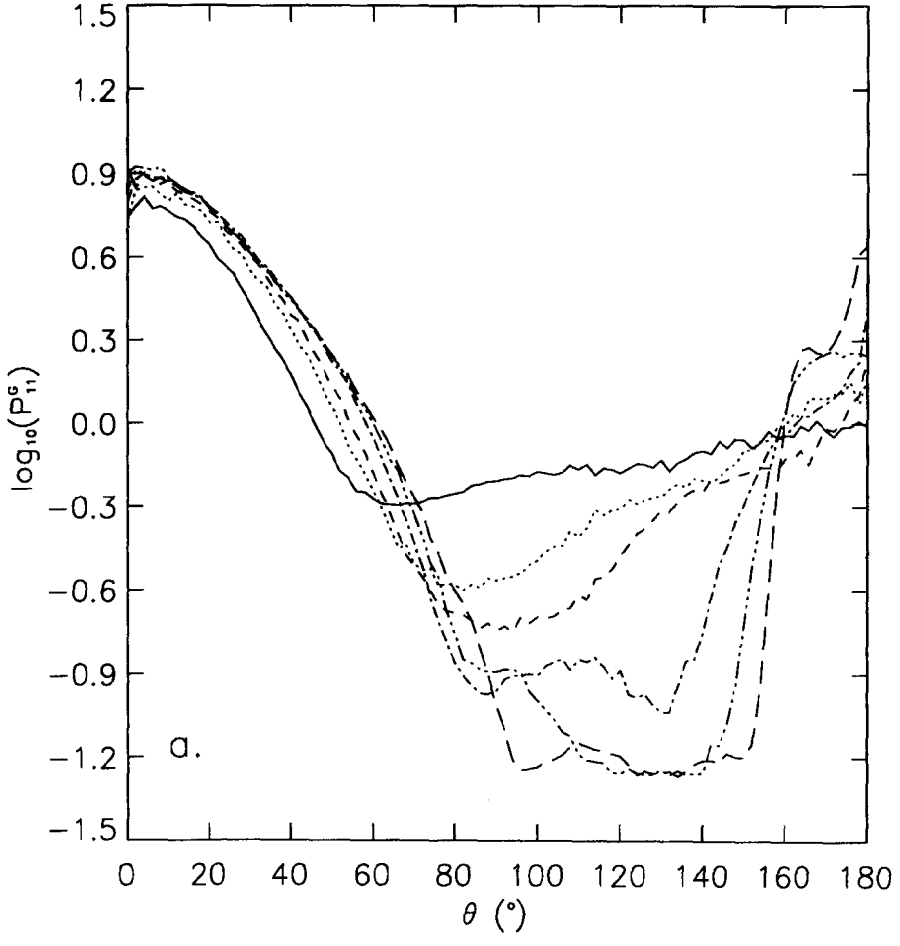

Fig. 4a

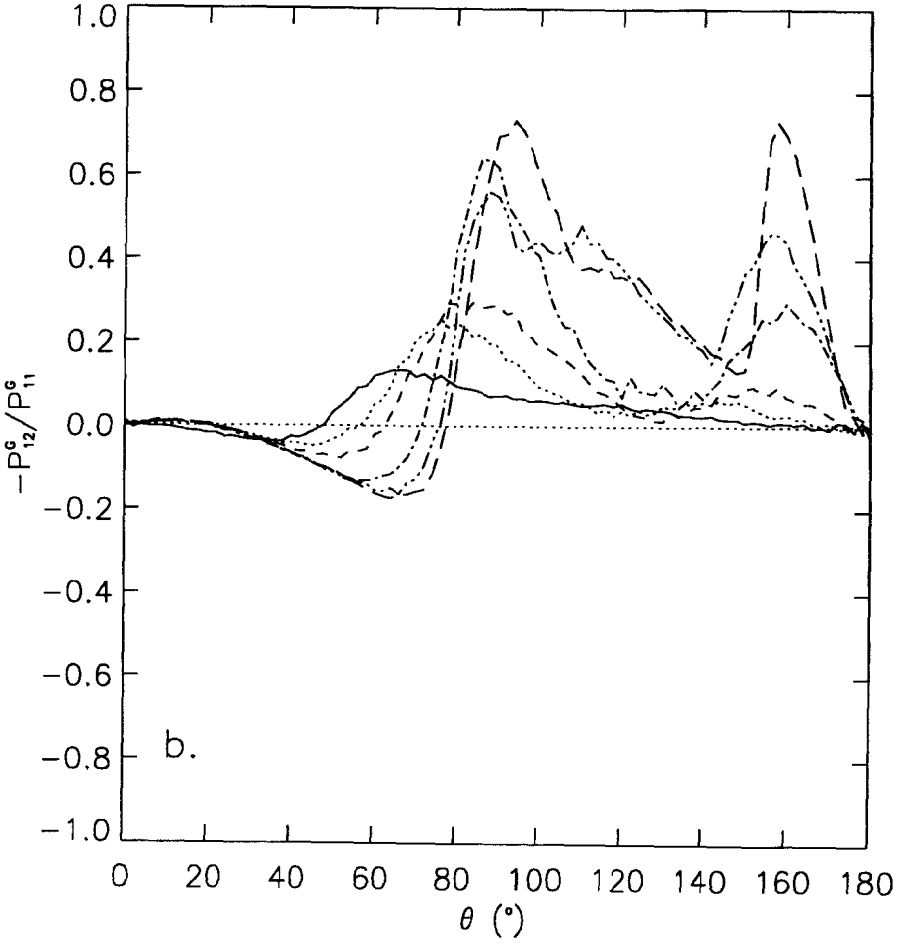

Fig. 4b

Fig. 4—*caption on p. 595*

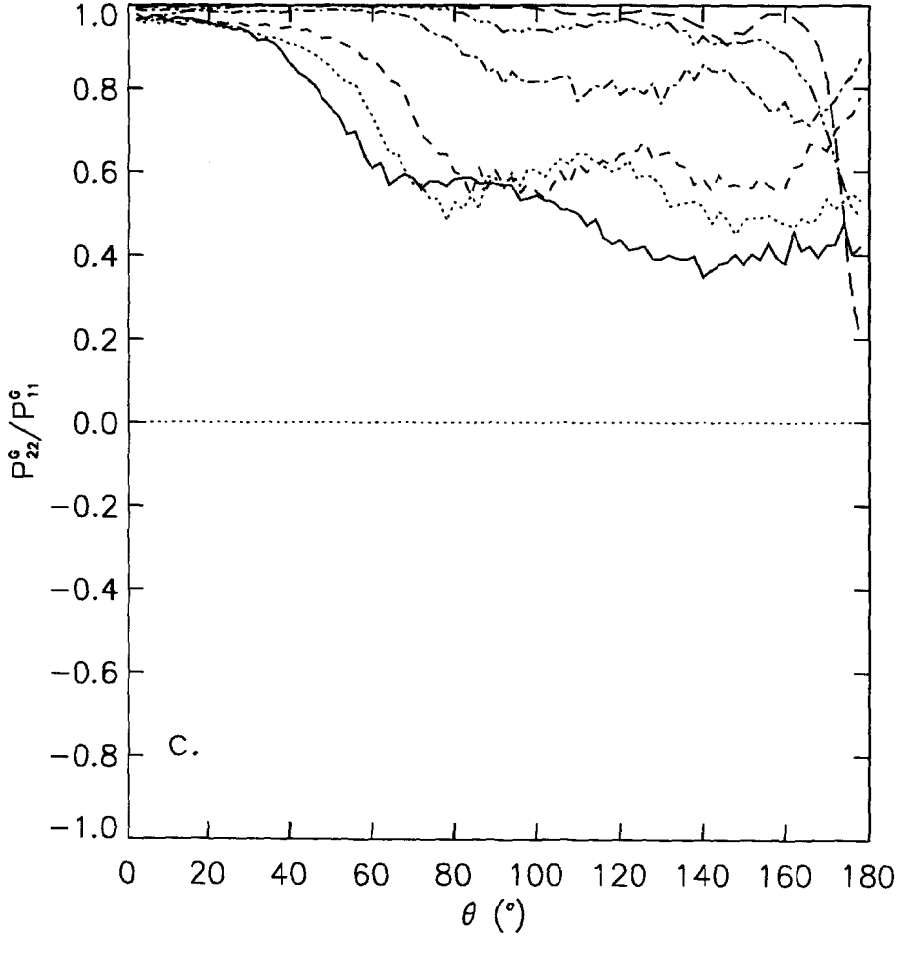

Fig. 4c

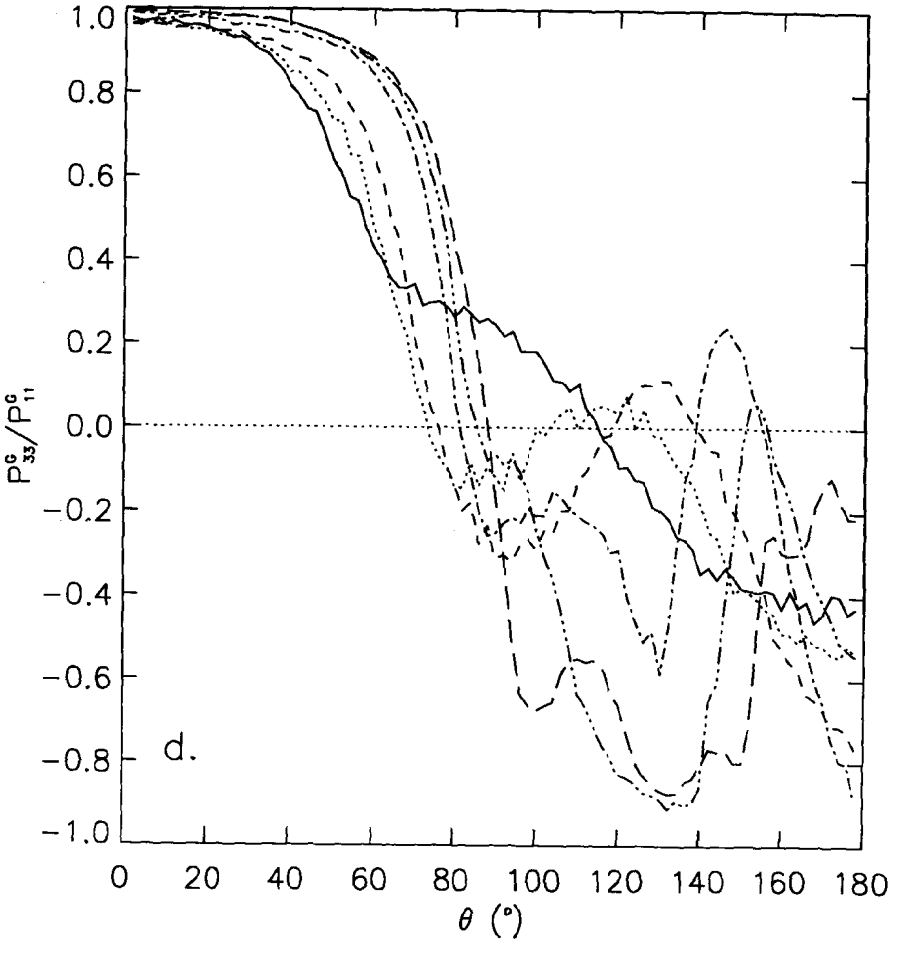

Fig. 4d

Fig. 4—*caption opposite.*

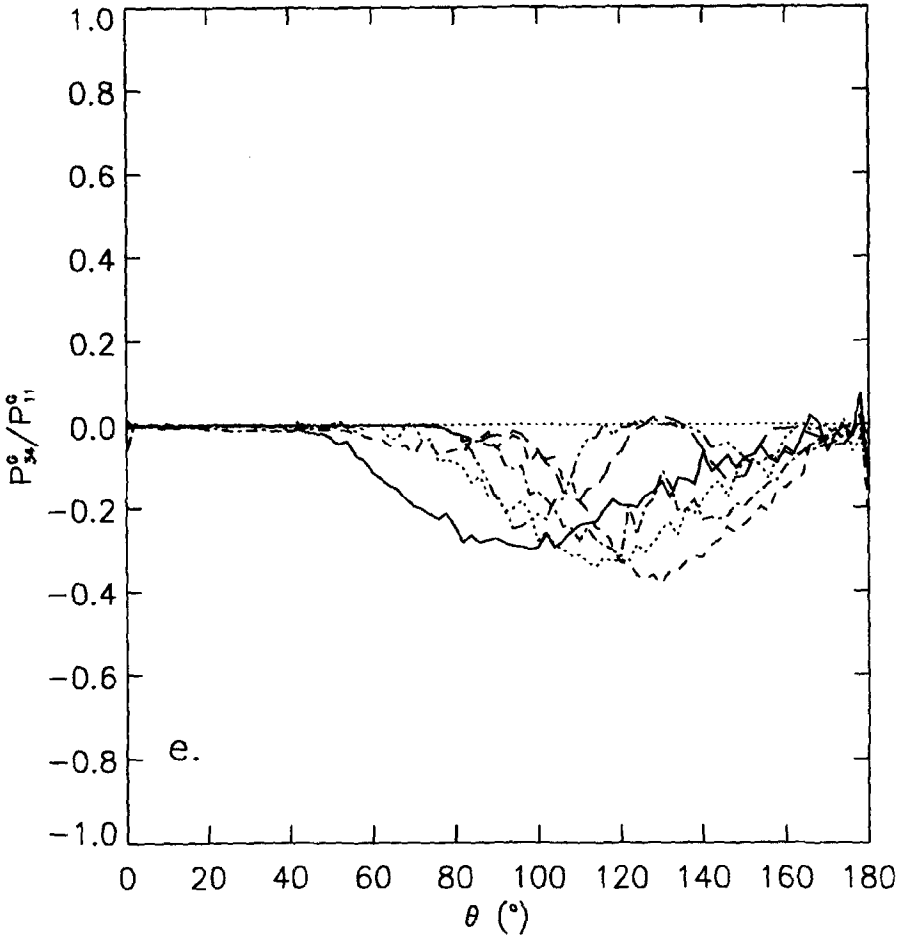

Fig. 4e

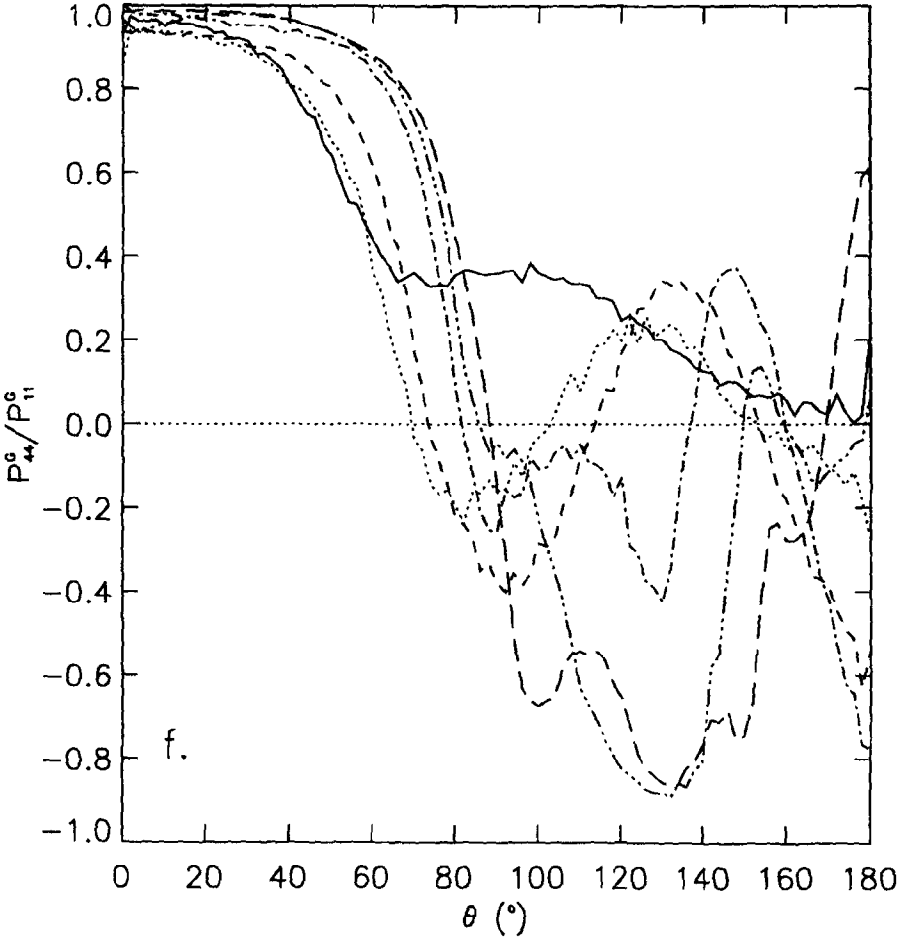

Fig. 4f

Fig. 4. Geometric optics scattering phase matrices for the refractive index $m = 1.55$ and standard deviation $\sigma = 0.10$. The different lines correspond to the correlation angles $\Gamma = 10°$ (——), 20° (· · · ·), 30° (– – – –), 60° (– · – · – · –), 90° (— · · · —), and 180° (— – – —). The matrix elements are as in Fig. 3.

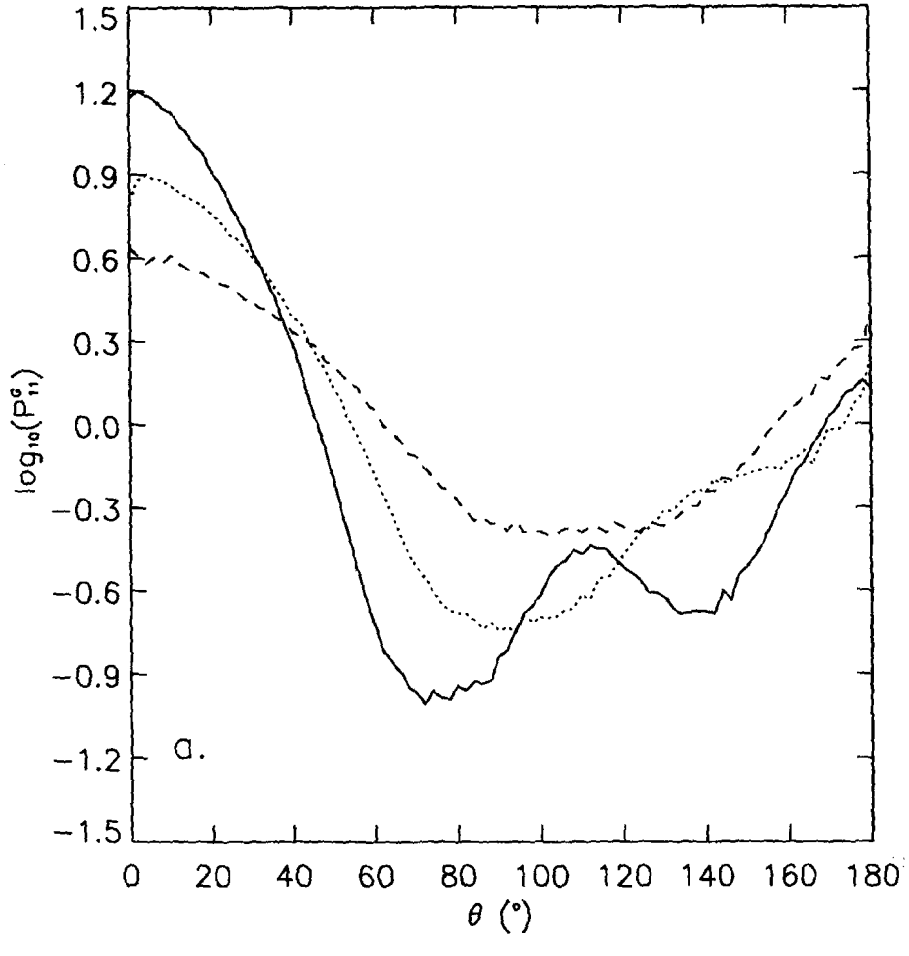

Fig. 5a

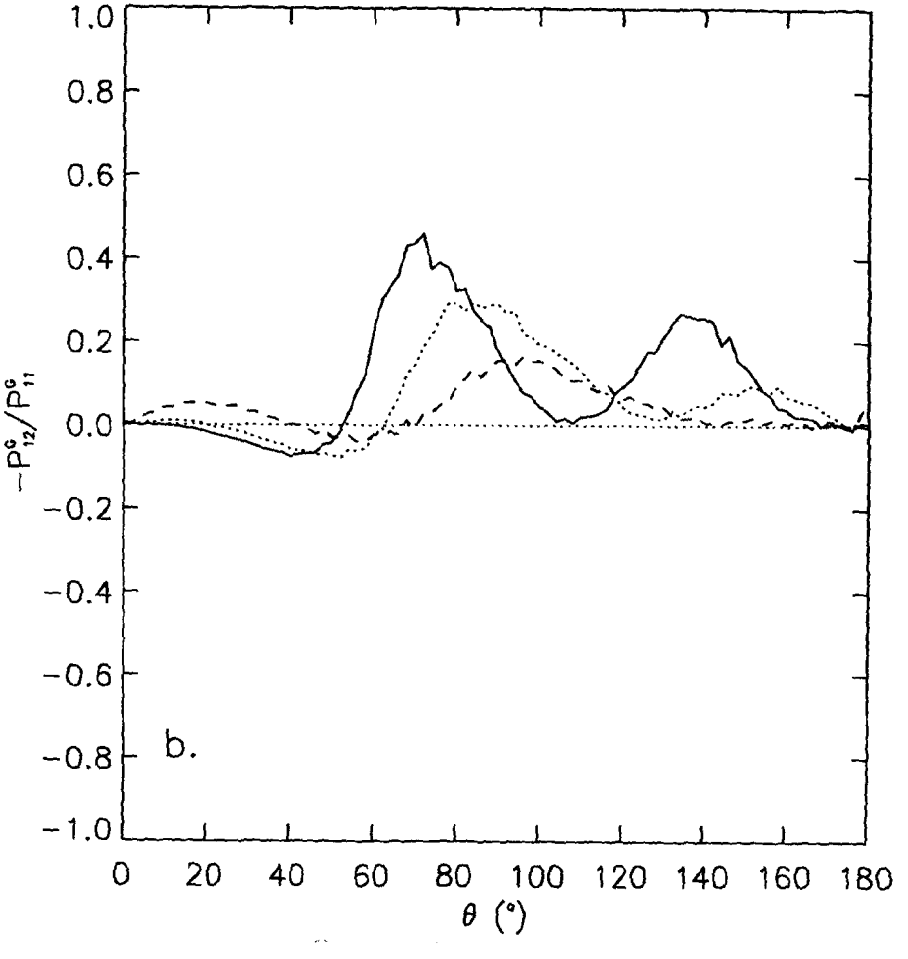

Fig. 5b

Fig. 5—*caption on p. 598*

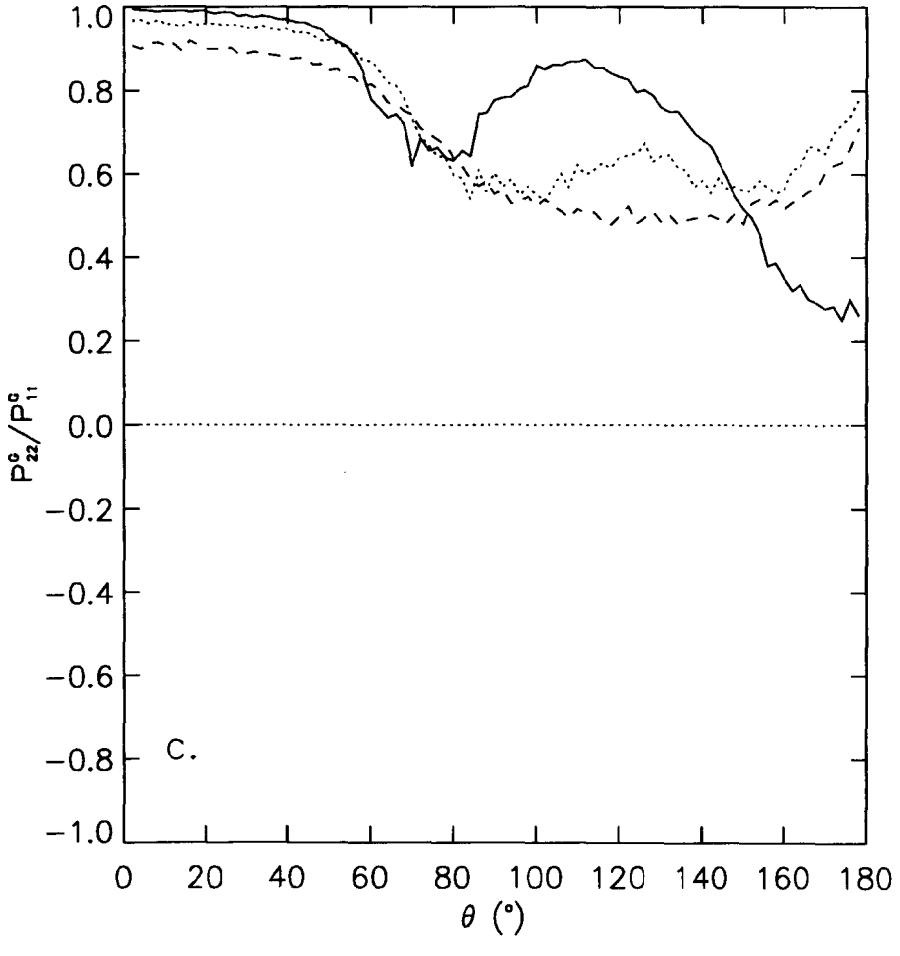

Fig. 5c

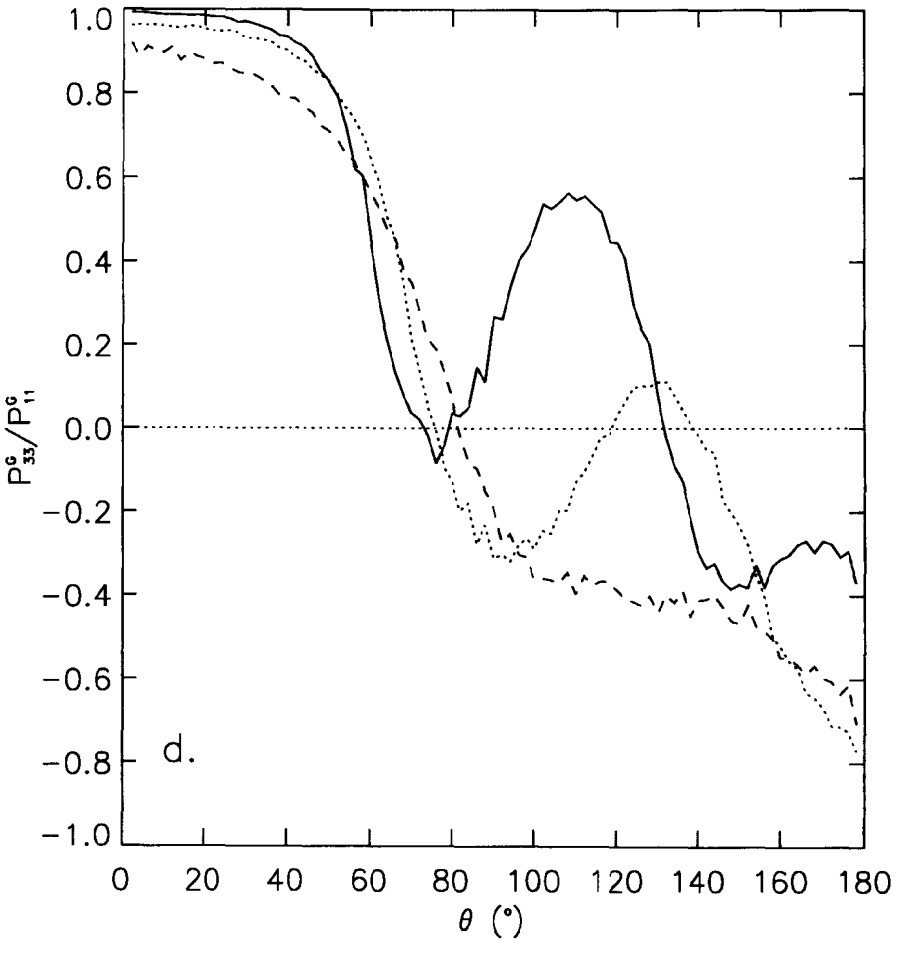

Fig. 5d

Fig. 5—*caption opposite.*

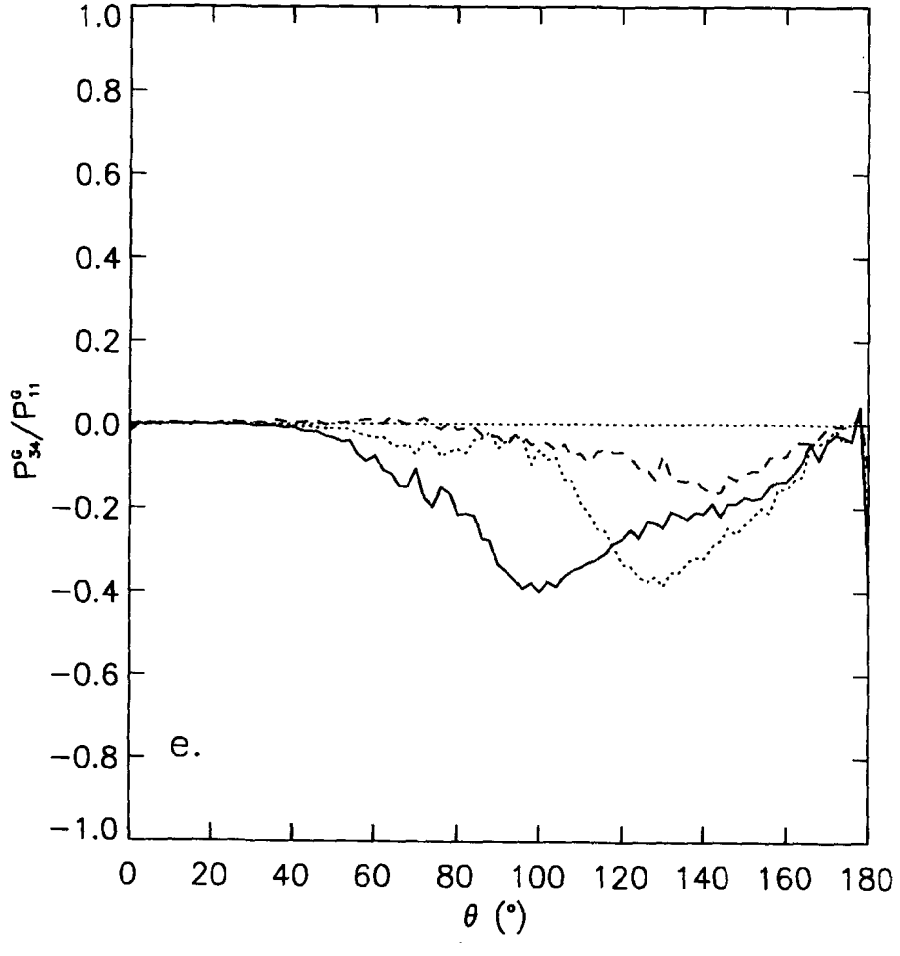

Fig. 5e

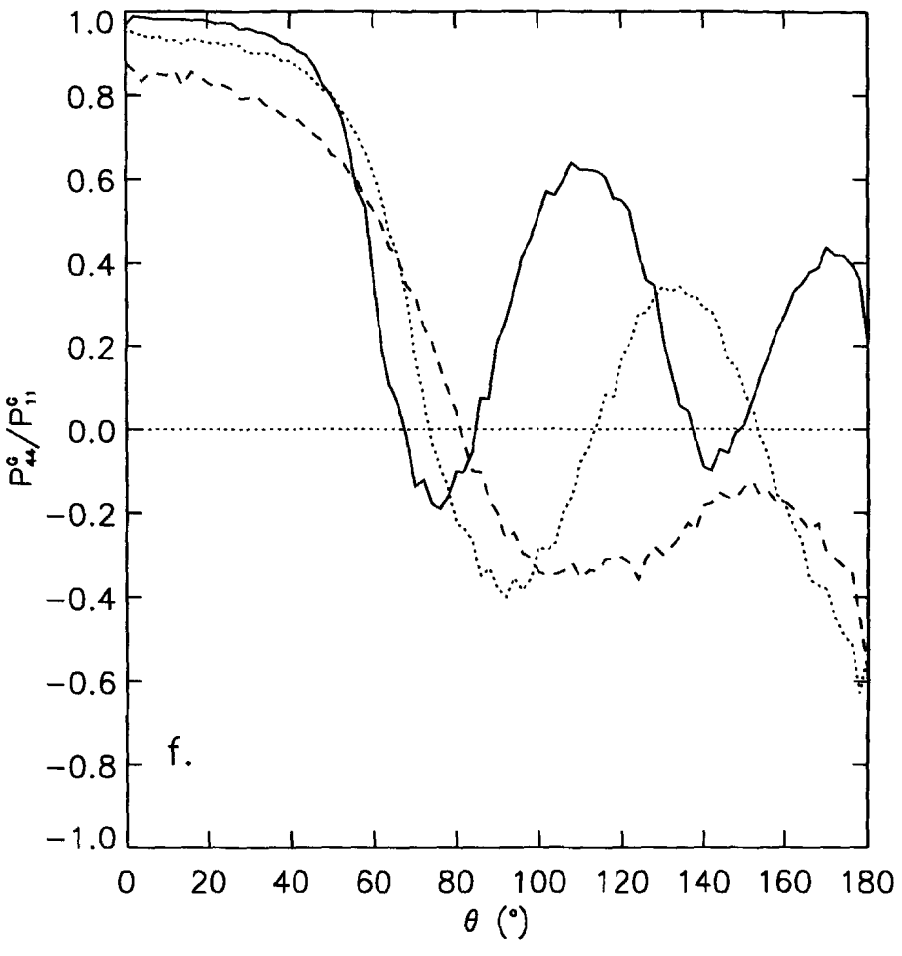

Fig. 5f

Fig. 5. Geometric optics scattering phase matrices for the standard deviation $\sigma = 0.10$ and correlation angle $\Gamma = 30°$. The different lines correspond to the refractive indices $m = 1.33$ (——), 1.55 (· · · ·), and 2.00 (– – – –). The matrix elements are as in Fig. 3.

5.1. P_{11}^G

For increasing standard deviation σ, the scattering phase function P_{11}^G tends to decrease in the forward scattering regime, in particular, for small correlation angles Γ. Also for increasing σ, the minimum at the intermediate scattering angles becomes shallower, the changes being smaller for larger σ. For small Γ, increasing σ tends to decrease the phase function in the backward scattering regime. [cf. Fig. 3(a).]

Increasing the correlation angle Γ systematically increases the phase function in the forward scattering regime, deepens the minimum at the intermediate scattering angles, and strengthens the backward regime. For the refractive index $m = 1.33$, backward scattering begins to decrease for the largest Γ: there is no glory for water droplets in the geometric optics approximation. For small σ, increasing Γ hardly affects the phase function. [cf. Fig. 4(a).]

Increasing Re(m) systematically decreases P_{11}^G in the forward scattering regime, and makes the minimum at the intermediate scattering angles shallower [Fig. 5(a)]. Increasing Im(m) systematically flattens the minima and maxima [Fig. 2(a)].

5.2. $-P_{12}^G/P_{11}^G$

For increasing standard deviation σ, the first and second polarization maxima at 50–90° and 100–160°, respectively, decrease, and the second maximum finally disappears. [cf. Fig. 3(b).]

In general, the correlation angle Γ strongly affects the shape of the polarization curve at the intermediate and backward scattering angles, whereas it hardly affects the forward scattering regime. For increasing Γ, the first maximum increases and moves backward. [cf. Fig. 4(b).]

Increasing Re(m) systematically neutralizes the polarization maxima [Fig. 5(b)], whereas increasing Im(m) leads to opposite behavior: the primary maximum increases [Fig. 2(b)].

5.3. P_{22}^G/P_{11}^G

For increasing standard deviation σ, P_{22}^G/P_{11}^G fairly systematically decreases. σ affects the curve shapes more for small refractive indices m. [cf. Fig. 3(c).]

The forward scattering regime is rather insensitive to changes in the correlation angle Γ and, in general, Γ affects the curve shapes less for larger m. For small m, the biggest changes due to Γ take place near the backward direction. [cf. Fig. 4(c).]

Increasing Re(m) destroys the local maximum at the intermediate scattering angles [Fig. 5(c)], whereas increasing Im(m) systematically increases the curve [Fig. 2(c)].

5.4. P_{33}^G/P_{11}^G

Increasing the standard deviation σ increases P_{33}^G/P_{11}^G at the intermediate scattering angles, whereas changes in the backward regime are usually small. For large refractive indices m, σ does not strongly affect the curve shape. [cf. Fig. 3(d).]

In general, the correlation angle Γ strongly affects the curve shape at the intermediate and backward scattering angles, whereas it hardly affects the forward scattering regime. However, for large m, increasing Γ leads to systematic increase in the forward scattering regime, and also deepens the minimum at the intermediate scattering angles. Increasing Γ tends to decrease the curves in the backward scattering regime. [cf. Fig. 4(d).]

Increasing Re(m) or Im(m) destroys the local maximum at the intermediate scattering angles [Figs. 2(d) and 5(d)].

5.5. P_{34}^G/P_{11}^G

For nonabsorbing particles, P_{34}^G/P_{11}^G is a measure of total internal reflection. For changing standard deviation σ, it does not behave systematically, though appears to be more insensitive for small refractive indices m. [cf. Fig. 3(e).]

Both the forward and backward scattering regimes are rather insensitive to changes in the correlation angle Γ. For small refractive indices m and large σ, the curves depend less on Γ. [cf. Fig. 4(e).]

Increasing Re(m) or Im(m) destroys the local minimum at the intermediate scattering angles [Figs. 2(e) and 5(e)].

5.6. P_{44}^G/P_{11}^G

For increasing standard deviation σ, P_{44}^G/P_{11}^G increases for large correlation angles Γ and, for small Γ, tends to decrease near the backward direction. The minimum at the intermediate scattering angles systematically increases for increasing σ. [cf. Fig. 3(f).]

In general, the curves strongly depend on Γ. For increasing Γ, the forward scattering regime increases, the backward scattering regime decreases, and the minimum at the intermediate scattering angles deepens. Increasing Γ tends to less and less affect the curves. [cf. Fig. 4(f).]

Increasing Re(m) or Im(m) destroys the local maximum at the intermediate scattering angles [Figs. 2(f) and 5(f)].

6. DISCUSSION

A great variety of random shapes can be generated using the lognormal statistics: they vary from modestly irregular to rough and extremely spiky shapes. The random shape can be applied to such diverse objects as asteroids and potatoes, for example. Convex Gaussian random particles can be generated using the convex hull concept for ordinary Gaussian random particles. Such particles can exhibit crystal-like outlook for large standard deviations of radius and small correlation lengths. In the present article, we have constrained ourselves to the modestly irregular shapes.

The concept of the Gaussian random particle is not limited to the spherical mean geometry. There are several ways of introducing elongation into the random particle. For example, elongated particles can be generated by giving larger standard deviations for the second-order spherical harmonics coefficients of the logradius. Or the basic random shape can be multiplied by an ellipsoidal shape. Furthermore, it is straightforward to extend the modeling to Gaussian random cylinders. Lognormal size distributions of spheres are often utilized for modeling scattering by small particles.[29] But such a distribution is, curiously, a Gaussian random particle with the autocorrelation function equal to unity.

In half-space problems, Gaussian statistics are often used to mark the boundary between the free space and particulate scattering medium. In full analogy, supported by the Central Limit Theorem, Gaussian random shapes can be used to describe the boundaries of fluffy single particles. After generating the boundary using the spherical harmonics method, the volume can be packed with, e.g., spheres of equal size, to the extent desired. Moreover, in the limit of small radius standard deviation and small correlation length, the lognormal statistics reduce to the Gaussian statistics. The Gaussian random surface in the planar geometry is thus a spherical case of the Gaussian random shape.

We plan to compare our ray optics results for Gaussian random particles to the Markovian approximation by Peltoniemi et al.[4] That approximation is considerably faster, but is a priori limited to Gaussian particles with small correlation angles. We will vary the autocorrelation function and examine its effects on the scattering parameters. We will also work toward a faster code for small correlation lengths and small standard deviations of the radius. We further aim to introduce the criteria by Hovenier et al[30] to verify our scattering phase matrices. One of our goals is to explain experimental results (e.g., Kuik et al[31] and Sasse et al[32]).

It is straightforward to modify the present ray tracing algorithm for any mathematically star-like geometries. We already programmed a code for ellipsoidal scatterers in order to compare the ray optics approximation to the T-matrix method[33] for light scattering by spheroidal particles.[34] We have recently established the Rayleigh and Rayleigh–Gans approximations for scattering by Gaussian random particles,[35] and hope to address the anomalous diffraction[36] and Kirchhoff approximations[26,27] in due course.

Acknowledgements—We are grateful to H. C. van de Hulst and M. I. Mishchenko for their constructive reviews, and to L. Lamberg and J. W. Hovenier for their crucial remarks. We thank J. Piironen for his art courtesy. The research was supported, in part, by the Academy of Finland.

REFERENCES

1. G. Mie, *Ann Phys.* **25,** 377 (1908).
2. Lord Rayleigh, *Phil. Mag.* **12,** 81 (1881).
3. E. Vanmarcke, *Random Fields: Analysis and Synthesis*, The MIT Press, Cambridge, MA (1983).

4. J. I. Peltoniemi, K. Lumme, K. Muinonen, and W. M. Irvine, *Appl. Opt.* **28,** 4088 (1989).
5. K. Muinonen, *Bull. Am. Astron. Soc.* **26,** 1173 (1994).
6. K. Muinonen, *Earth, Moon and Planets* **72,** 339 (1996).
7. S. Mukai, T. Mukai, K. Weiss, and R. H. Zerull, *Moon and Planets* **26,** 197 (1982).
8. R. Schiffer, and K. O. Thielheim, *Astron. Astrophys.* **116,** 1 (1982).
9. M. Bottlinger and H. Umhauer, *Appl. Opt.* **30,** 4732 (1991).
10. E. A. Hovenac, *Appl. Opt.* **30,** 4739 (1991).
11. R. Schiffer, *Astron. Astrophys.* **148,** 347 (1985).
12. R. Schiffer, *JOSA A* **6,** 385 (1989).
13. R. Schiffer, *Appl. Opt.* **29,** 1536 (1990).
14. E. Bahar and M. A. Fitzwater, *JOSA A* **5,** 89 (1988).
15. D. J. Schertler and N. George, *JOSA A* **11,** 2286 (1994).
16. S. L. César, E. F. Vasconcelos, V. N. Freire, and G. A. Farias, in *Eighth Conf. on Atmospheric Radiation*, Preprints, 350, Nashville, TN (1994).
17. P. C. Waterman, *Phys. Rev. D* **3,** 825 (1971).
18. M. I. Mishchenko, *JQSRT* **55,** 535 (1996).
19. S. Asano and G. Yamamoto, *Appl. Opt.* **14,** 29 (1975).
20. N. V. Voshchinnikov, *JQSRT* **55,** 627 (1996).
21. K. Lumme and J. Rahola, *Astrophys. J.* **425,** 653 (1994).
22. B. Michel, *JOSA A* **12,** 2471 (1995).
23. J. I. Peltoniemi, *JQSRT* **55,** 637 (1996).
24. K. Muinonen, M.Sc. thesis, Univ. of Helsinki (1986).
25. K. Muinonen, K. Lumme, J. I. Peltoniemi, and W. M. Irvine, *Appl. Opt.* **28,** 3051 (1989).
26. K. Muinonen, *Appl. Opt.* **28,** 3044 (1989).
27. J. D. Jackson, *Classical Electrodynamics*, Wiley, New York, NY (1975).
28. W. H. Press, B. P. Flannery, S. A. Teukolsky, and W. T. Vetterling, *Numerical Recipes, The Art of Scientific Computing*, Cambridge Univ. Press, Cambridge, MA (1986).
29. J. E. Hansen and L. D. Travis, *Space Sci. Rev* **16,** 527 (1974).
30. J. W. Hovenier, H. C. van de Hulst, and C. V. M. van der Mee, *Astron Astrophys.* **157,** 301 (1986).
31. F. Kuik, P. Stammes, and J. W. Hovenier, *Appl. Opt.* **30,** 4872 (1991).
32. C. Sasse, K. Muinonen, J. Piironen, and G. Dröse, *JQSRT* **55,** 673 (1996).
33. M. I. Mischenko, *Opt. Comm.* **109,** 16 (1994).
34. A. Macke, M. I. Mishchenko, K. Muinonen, and B. Carlson, *Opt. Lett.* **20,** 1934 (1995).
35. K. Muinonen, *JQSRT* **55,** 577 (1996).
36. H. C. van de Hulst, *Light Scattering by Small Particles*, Wiley, New York, NY (1957).